



Contents

- [Effect of Inner Body Shapes on Natural Convection in Square Enclosures](#)
- [Thermodynamic and Mechanistic Insights into Paracetamol Removal from Aqueous Solutions by Graphitic Carbon Nitride Nanosheets](#)
- [Analysis of Magnetic Properties and Critical Current Density of Tl-2234 High-Temperature Superconductor Using AC Magnetic Susceptibility Measurements](#)
- [Ab Initio Study of Structural, Thermal Stability and Electronic Properties of LiRuPO₄ Compound: A Storage Energy Application](#)
- [Effect of thermal configurations in multi-pipe heat exchangers on MHD natural convection within a square enclosure with curved corners](#)
-



Effect of Inner Body Shapes on Natural Convection in Square Enclosures

Wedad Hassan Asiri ¹, Ammar Abdulkadhim ², Halemah Ibrahim Elsaeedy ¹, Nejla Mahjoub Said ^{1,*}

¹ Department of Physics, College of Science, King Khalid University, Abha 61413, Saudi Arabia,
445816980@kku.edu.sa; halsayed@kku.edu.sa; nalmahjoub@kku.edu.sa

² Mechanical Engineering Department, University of Al-Qadisiyah, Al-Qadisiyah 58001, Iraq,
ammar.abdulkadhim@qu.edu.iq

*Corresponding author: (N. Mahjoub), *Email Address:* nalmahjoub@kku.edu.sa

Abstract

This review focuses on the effects of inner body shapes on magnetohydrodynamic (MHD) natural convection heat transfer within square enclosures, summarizing advancements from 2015 to 2024 and identifying future research directions. The influence of different geometric shapes such as circular, square, triangular, and elliptical on heat transfer performance and flow behavior is critically examined. The review also addresses the roles of Rayleigh and Hartmann numbers in modulating convection characteristics in the presence of a magnetic field. Key trends and findings are highlighted, along with observed research gaps, to guide future studies aiming to enhance thermal management in MHD driven systems.

Keywords: Natural convection, magnetic field, square enclosures, inner bodies, hartmann number.

<https://doi.org/10.63070/jesc.2025.001>

Received 16 March 2025; Revised 25 April 2025; Accepted 03 May 2025.

Available online 15 May 2025.

Published by Islamic University of Madinah on behalf of *Islamic University Journal of Applied Sciences*. This is a free open access article.

1. Introduction

Natural convection is a critical heat transfer process driven by fluid motion from internal forces rather than external sources. This motion arises from buoyancy effects, where temperature-induced density gradients in the fluid initiate flow. Natural convection plays a vital role in numerous applications in engineering, including electrical component cooling, building insulation, solar energy systems, heat exchangers, material drying, and thermal storage. Unlike forced convection, it operates without input of external energy, which makes it inherently energy efficient. Understanding the mechanics of natural convection and evaluating thermal performance are therefore crucial for optimizing these systems. Due to the intricate interactions between the fluid and boundary layers on horizontal and vertical surfaces, this phenomenon presents a complex internal flow problem. A wealth of studies have explored natural convection's heat transfer processes across diverse fields, each aiming to enhance specific performance outcomes [1].

Nanofluids, comprising nanoparticles suspended in base fluids such as water or oil, exhibit enhanced thermal properties that surpass those of conventional fluids. These specialized fluids play a crucial role in advancing heat transfer across various high-demand industrial applications, including solar energy systems, nuclear reactors, and high-performance electronic devices. Their effectiveness in electronic cooling, particularly for critical components like microprocessors, enables sustained high-efficiency performance. The stable dispersion of nanoparticles within the fluid prevents common issues like sedimentation and conduit blockages, which are often associated with larger particles. Future research into nanofluids is anticipated to further enhance thermal efficiency, leading to the development of more compact and efficient heating and cooling systems across industries [2].

Kasaeian et al. [3] have highlighted an important focus in the field of heat transfer, particularly in exploring methods to enhance the performance of energy devices. Among the recent techniques investigated for this purpose are using nanofluids and porous media within heat exchangers. Nanofluids are defined as suspensions of solid nanoparticles in base fluids, such as water. This paper provides a thorough analysis of various studies examining the combined application of nanofluids and porous media within thermal systems, considering diverse geometrical structures and flow regimes.

Das et al. [4] examine internal natural convection heat transfer enclosures characterized by triangular, trapezoidal, parallelogrammatic, and curved walls, incorporating both fluids and porous media. The study also explores enclosures filled with nanofluids. Key parameters such as aspect ratio and the base angle of triangular and rhombic/parallelogrammatic enclosures significantly impact flow distribution. Furthermore, flow patterns are influenced by the number of undulations in the walls and the amplitude-to-wavelength ratio. The review highlights

various strategies aimed at enhancing convection heat transfer performance, providing valuable insights into potential improvement techniques in this area.

Biswal and Basak [5] present a comprehensive review focusing on the investigation of entropy production in natural convection across a range of applications and geometries. The review elucidates the mathematical formulation of fundamental equations, calculation procedures, and methodologies for conducting thorough evaluations. A central challenge addressed is the trade-off between minimizing entropy generation and maximizing heat transfer rates for optimal configurations that enhance energy efficiency. The process of natural convection is crucial for converting renewable energy into usable forms, making the analysis of entropy production an essential consideration in the design of effective energy systems. Furthermore, the article offers insights and discussions aimed at guiding future research on improving energy efficiency within renewable energy systems.

Sadeghi et al. [6] provide a comprehensive review of recent literature on the natural convection of nanofluids across various container geometries, including triangular, trapezoidal, square, circular, and non-traditional forms. The study explores the relationship between thermophysical properties and the geometric configuration of the cases, employing numerical methods and microscopic models to support their findings.

Giwa et al. [7] investigate the control of Heat transmission via spontaneous convection and the flow characteristics of nanofluids in square cavities utilizing magnetic field sources. The study examines the influence of various parameters, For the magnetohydrodynamic (MHD) behaviors of natural convection, these include heat distribution techniques, thermal and concentration boundary conditions, governing parameters, magnetic field types, numerical schemes, thermophysical correlations, nanofluid types, slip conditions, Brownian motion, and thermophoresis.

Hemmat et al. [8] review of natural convective heat transfer in nanofluid-filled cavities influenced by Magnetic Fields (M.F). The paper provides an introduction to nanofluids and their applications, along with an evaluation of numerical studies on magnetic nanofluids. It classifies the literature based on common geometries and effective parameters relevant to nanofluids under free convection and magnetic field effects. The findings indicate that when the magnetic field strength increases, the rate of heat transmission falls.

As the field of natural convection continues to evolve, numerous researchers have contributed to the understanding of heat transfer mechanisms in various geometries and configurations. These studies have significantly advanced our knowledge, exploring factors such as the impact of nanofluids, geometric shapes, and magnetic fields on natural convection performance. The following section will highlight key findings and methodologies from previous studies, offering a comprehensive overview of the advancements in this area.

2. The most selected parameters in the previous publications

A substantial body of literature discusses natural convection in square enclosures, looking at a number of variables such as the Rayleigh number (Ra), which quantifies the ratio of buoyancy forces to viscous forces. Studies, including those conducted by Chen et al. [9], have demonstrated that increasing the Rayleigh number correlates with an enhanced pace at which heat is transferred by natural convection.

Flow patterns and the amount of heat transferred are significantly influenced by the Rayleigh and Hartmann numbers, which serve as critical variables in determining flow behavior; an increase in the Rayleigh number results in more complex flow structures and consequently enhances the heat transfer rate. Studies by Chen et al. [9] show that because a magnetic field inhibits fluid motion, raising the Hartmann number (Ha) lowers heat transfer rates within square cavities. [9, 10]. Numerical modeling and experimental analysis are essential for understanding these dynamics. Techniques For example, the Finite Volume Method (FVM) and the Finite Element Method (FEM) offer valuable predictive insights into temperature variations within the cavity under changing parameters. However, experimental validation is necessary to ensure the reliability of numerical results against actual data, thus enhancing the credibility of the findings [9, 10].

2.1. Conventional Square enclosure in the absence of the magnetic field

Joshi and Pattamatta [11] conducted an experimental investigation on buoyancy induced Using AL_2O_3 /Water and MWCNT/Water nanofluids in a square cavity for convective heat transfer. Their findings revealed that the MWCNT/Water nanofluid exhibited higher Nusselt numbers compared to the AL_2O_3 /nanofluid of water at certain volume fractions. The volume ratios used to create the MWCNT/Water nanofluid were 0.1%, 0.3%, and 0.5%.and the study analyzed its performance across a Rayleigh number range from 7×10^5 to 1×10^7 .

Hidayathulla et al. [12] conducted Examining unstable heat and momentum transfer numerically in a Newtonian fluid that fills a square hole. Their analysis the governing equations are solved using the Harlow-Welch Marker and Cell (MAC) finite difference method. In their study, they varied the thermal Grashof number (Gr) while maintaining a Prandtl number (Pr) of 0.7 (for air) and a Reynolds number (Re) of 10, indicating laminar flow conditions.

Khatamifar et al. [13] investigated the heat transfer from transient conjugate natural convection in a differentially heated cavity numerically, considering the effects of finite partition thickness and thermal conductivity. The study explored a range of Rayleigh numbers (Ra) from 10^3 to 10^8 , with dimensionless partition thicknesses between 0.05 and 0.2 and the partition's thermal conductivity ratio to the liquid between 0.1 and 1000. The results illustrate the transient development of natural convection flow within the partitioned cavity for various values of Ra (10^3 , 10^4 , 10^5 , 10^6 , 10^7 and 10^8), k_r (0.1, 1, 10, 100, 500 and 1000) and T_p (0.05, 0.1 and 0.2), all maintaining a constant $X_p = 0.5$, $H/L = 1$, and Prandtl number (Pr) of 0.71.

Kumar et al. [14] investigated the beginning of the free thermal flow of a silver nanofluid in a closed square chamber with isothermal vertical walls at different temperatures and adiabatic horizontal walls filled with a saturated porous media. Using the Boussinesq approximation and the Darcy model, they used a two-temperature nonequilibrium model to construct the governing boundary layer equations. Setting $\Gamma = 1$, $\gamma = 1$, $H = 10$, $Ra = 100$, and $R_d = 0.3$ as default settings for the emerging flow parameters was done by the study.

2.2. Conventional Square Enclosure without Inner Body in the Presence of a Magnetic Field

Many researchers have examined the impact of magnetic fields on natural convection heat transfer within square enclosures. For instance, Mansour and Bakier [15] a computational investigation of the flow of nanofluids and the heat transfer related to natural convection in the presence of an angled magnetic field and varied thermal boundary conditions. They looked into a lot of different things, like the heat source's length ($0.2 < B < 0.8$), its location ($0.3 < D < 0.7$), the solid volume fraction ($0 < \phi < 0.2$), the inclination angle ($0 < \Phi < 90^\circ$), the Rayleigh number ($10^3 < Ra < 10^5$), the Prandtl number ($Pr = 6.2$), and the Hartmann number ($0 < Ha < 100$). The results indicated that the inclination angle significantly affects heat distribution; as the angle increases, convection is enhanced, and the presence of nanoparticles improves conduction, thereby increasing the heat transfer rate. The study concluded that the temperature distribution within the cavity is influenced solely by the volume fraction of nanoparticles, a finding supported by numerous prior studies.

Furthermore, the article presents a numerical investigation of natural convection under the influence of magnetic fields in a square container containing an ethylene glycol-copper nanofluid, employing COMSOL Multiphysics for simulation. The authors concluded that the impact of the Hartmann number on the y-directional velocity component are more pronounced than those of the Rayleigh number. With a Prandtl number set at $Pr = 151$, they inspected the impacts of the relevant parameters, specifically the Rayleigh and Hartmann numbers, on the flow dynamics and heat transfer performance within the enclosure. The study also highlighted that enhanced ethylene glycol nanofluids exhibited superior thermal conductivity compared to other nanoparticles, as noted by Ben Hamida and Charrada [16].

Sreedevi and Reddy [17] looked over heat transport by natural convection in a square cavity with a Tiwari-Das nanofluid model, considering magnetic field and thermal radiation. The system's nonlinear partial differential equations were solved using the finite difference method. Their study investigated the impact of a number of critical parameters on the flow and heat transfer properties of the TiO_2 -EG nanofluid, such as the volume fraction ($0.01 \leq \phi \leq 0.09$), the magnetic field parameter ($1.0 \leq M \leq 3.0$), the Rayleigh number ($100 \leq Ra \leq 1000$), the radiation parameter ($0.1 \leq R \leq 0.9$), the Reynolds number ($0.1 \leq Re \leq 0.5$), the Prandtl number ($1.0 \leq Pr \leq 7.2$), and the Prandtl number ($5.2 \leq Pr \leq 7.2$). Graphs show how these factors affect the behavior of nanofluids and how they affect the performance of heat transfer and flow.

Haritha et al. [18] analyzed free convection heat transfer in a porous medium-filled square cavity saturated with nanofluids containing various nanoparticles, under the influence of an applied magnetic field and viscous dissipation. Using Darcy's model, they applied the finite element method based on the weighted Galerkin residual scheme to solve the governing equations. Parameters included Rayleigh number ($Ra = 50, 200, 800$), magnetic field parameter ($M = 0.5, 1, 1.5$), and nanofluid volume fraction ($\phi = 0.02, 0.2, 0.6$). The study found that heat transfer and flux density were highest with Cu nanoparticles and lowest with AL_2O_3 , with Figure 1 illustrating changes in heat transfer for varying Eckert numbers and volume fractions of nanoscale copper ($\phi = 0.02, 0.2, 0.6$).

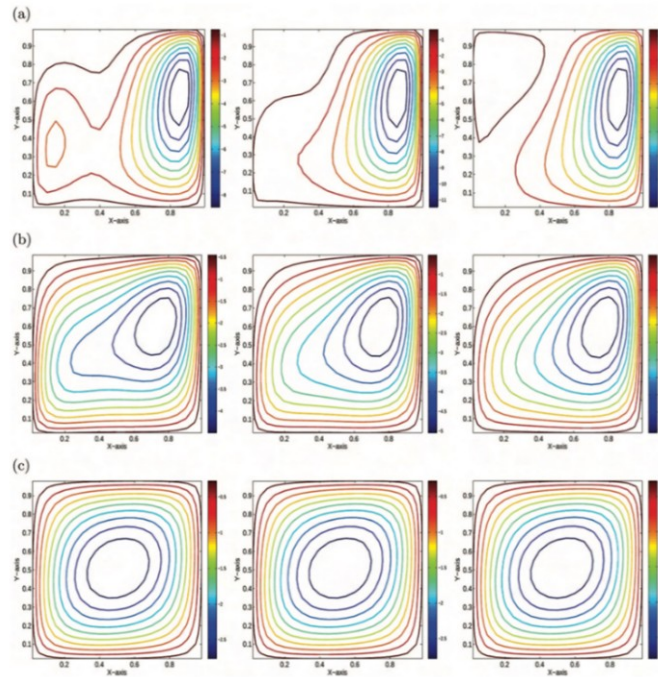


Figure 1. streamlines with $Ec = 0.01, 0.02,$ and 0.03 and $\phi = 0.02, 0.2,$ and 0.6 , respectively [18].

Mehryan et al. [19] showed how a periodic magnetic field affected the Fe_3O_4 nanofluid's natural convection and entropy production in a square cavity. To solve the governing partial differential equations, they used the Galerkin finite element method, concentrating on dimensionless parameters like the nanoparticle volume fraction ($\phi = 0-0.08$), period number ($\lambda = 0.1 - 1.0$), Rayleigh number ($Ra = 10^3-10^6$), and Hartmann number ($Ha = 0-50$), which indicates the amplitude of the magnetic field. The results showed that total entropy production (St) under the periodic magnetic field was higher than that under a uniform magnetic field, regardless of Ha and λ values.

Mansour et al. [20] treated entropy generation, MHD convective flow, and heat transfer in a square porous cavity. Using finite difference methodology, they assessed parameters such as the magnetic field ($0 \leq Ha \leq 100$), heat source ($-4.0 \leq Q \leq 4.0$), volume fraction of nanoparticles ($0.03 \leq \phi \leq 0.1$), and permeability ($10^{-6} \leq Da \leq 10^{-2}$).

Their findings showed that adding copper nanoparticles achieved the highest heat transfer rates among the materials tested.

Al Kalbani et al. [21] studied the effects of a directed magnetic field on the heat transfer and fluid flow properties of natural convection in an inclined square container filled with different nanofluids containing different forms of nanoparticles. The governing non-dimensional partial differential equations were solved using the weighted Galerkin residual finite element technique. Their study considered different values for the following: inclination angle ($0^\circ \leq \delta \leq 90^\circ$), Hartmann number ($0 \leq Ha \leq 60$), magnetic field orientation ($0^\circ \leq \gamma \leq 90^\circ$), Rayleigh number ($10^3 \leq Ra \leq 10^6$), and nanoparticle volume percent ($0 \leq \phi \leq 0.05$).

Mahapatra and Parveen [22] analyzed spontaneous convection flow in a copper-water nanofluid-filled container with a sinusoidal top wall that was differentially heated and subjected to a continuous vertical magnetic field. A constant Prandtl number of $Pr = 6.2$ was maintained throughout their investigation as they investigated a number of parameters, such as Rayleigh number ($10^2 \leq Ra \leq 10^6$), sinusoidal wall amplitude ($0 \leq a \leq 0.4$), nanoparticle volume fraction ($0.0 \leq \phi \leq 0.2$), and Hartmann number ($0 \leq Ha \leq 50$), using the Bi-CGStab method for numerical simulations. Increasing the Rayleigh number from 10^2 to 10^4 improved flow strength, heat transfer rate, and entropy formation, according to their findings, both with and without magnetic fields.

Uddin et al. [23] assessed natural convection heat transfer using a heterogeneous dynamical model in a square jar filled with a copper oxide nanofluid, exposed to a uniform magnetic field, and having a wavy top wall. They discussed the effects of several control parameters on the flow and thermal fields, such as Hartmann number, magnetic field inclination angle, gravitational inclination angle, solid volume fraction, nanoparticle diameter, and dimensionless time, by applying the Galerkin finite element method to the governing equations. Their study's main goal was to assess the improvement in heat transmission under various parameter combinations for real-world uses.

Rajarathinam and Chamkha [24] investigated the effects of partial convection in a water-based nanofluid within a square cavity subjected to a magnetic field. They addressed the governing unstable non-dimensional partial differential equations using the SIMPLE algorithm in conjunction with the finite volume method. Their results, presented in Figure 2, encompass various relevant parameters, including the Hartmann number ($0 \leq Ha \leq 100$), Rayleigh number ($10^2 \leq Ra \leq 10^6$), solid volume fraction ($0.0 \leq \phi \leq 0.04$), and three distinct opening configurations. The study reveals that the vertical velocity component at the cavity's center achieves its maximum when both buoyancy forces and velocity boundary conditions are absent, influencing the flow behavior across all positions.

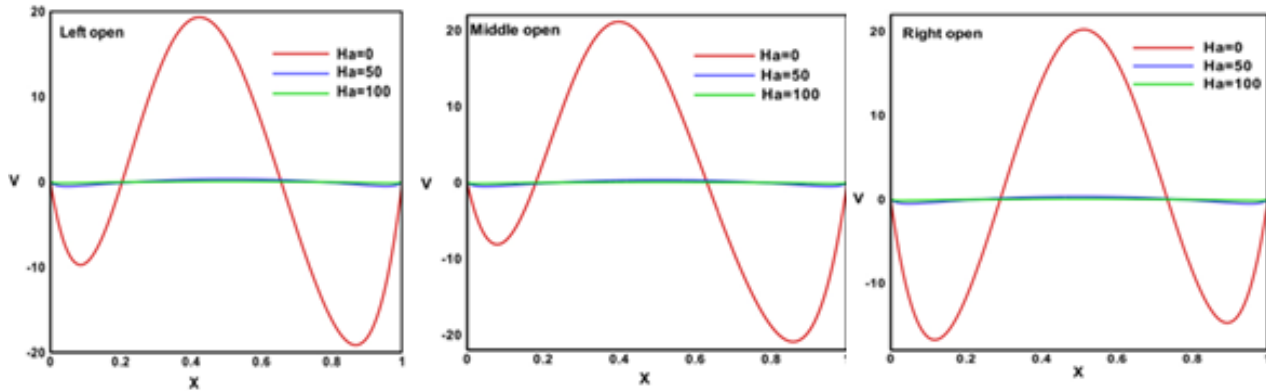


Figure 2. Vertical velocity profiles for various Hartmann numbers and opening positions at $Y=0.5$, with $Ra = 10^4$ and $\phi = 0.02$. [24]

Devi et al. [25] explored the influence of magnetic wire on the viscous Casson flow in a container with opposing temperature gradients and cadaveric upper and lower walls, utilizing the MAC technique for numerical analysis. The work concentrated on controlling the following fluid flow parameters: Casson fluid parameter $\beta = 0 - \infty$, Hartmann number (0 - 8), Rayleigh number ($10^3 - 10^5$), and a constant Prandtl number $Pr = 6.8$. According to their research, buoyant force causes the temperature gradient to rise.

Nishad et al. [26] analyzed heat transfer and flow in a copper-water nanofluid-filled undulating container while subjected to a magnetic field using a parallel grid-free method. Using the element-free Galerkin method (EFGM), the equations governing the transport phenomena were numerically solved. Their findings were obtained for a number of parameters, such as the magnetic field inclination angle ($0^\circ \leq \theta \leq 80^\circ$), nanoparticle volume fraction ($0 \leq w \leq 0.5$), Rayleigh number ($10^3 \leq Ra \leq 10^5$), and Hartmann number ($0 \leq Ha \leq 60$). The study found that a greater Hartmann number Lorentz force suppresses fluid motion and lowers the cavity's heat transfer rate, which in turn reduces stream functions.

2.3. Previous studies with inner Bodies

2.3.1 Square inner Body

Munshi et al. [27] performed a numerical analysis of a square's natural convection container characterized by an irregularly unheated bottom wall and a hot mass in the shape of a square. They explored the influence of various Prandtl numbers (0.71, 1.0, and 1.5) on Heat transmission and fluid flow within the enclosure. Their parametric analysis revealed that as the Prandtl number increases, free convection is suppressed, leading to a predominance of heat transmission via conduction. The results indicated that the heat transfer processes, temperature distribution, and flow characteristics inside the cavity are significantly influenced by the Rayleigh number as well as the magnetic field's strength.

Boulaiah et al. [28] performed a numerical investigation into the natural thermal transfer of a nanofluid (Cu-water) within a square enclosure containing a cold rectangular obstacle. They employed the finite difference method to solve the transport equations using the Alternating Direction Implicit (ADI) approach. Their study identified several dimensionless groups, including the height of the obstacle ($0.125 \leq H \leq 0.5$), the Rayleigh number ($10^3 \leq Ra \leq 10^6$), and the volume fraction of nanoparticles ($0 \leq \phi \leq 0.2$), while maintaining the obstacle's width at $0.25L$ and the Prandtl number for pure water at $Pr = 6.2$. The findings demonstrated that heat transfer was enhanced by increasing both the Rayleigh number and the volume fraction of nanoparticles.

2.3.2 Elliptical inner body

Munshi et al. [29] examined how fluid flow and heat transfer were affected by magnetohydrodynamic (MHD) natural convection in a square cavity that held an electrically conducting fluid with an elliptical adiabatic mass. Using numerical techniques, the study produced predictions over a wide range of Hartmann numbers (Ha) and Rayleigh numbers (Ra) while keeping the Prandtl number constant at 0.733 . The governing equations pertaining to the parameters of heat production were solved using the finite element method. The findings indicated that an increase in the Rayleigh number enhances the buoyant force, necessitating a stronger magnetic field to reduce natural convection effects, particularly at lower Rayleigh numbers.

Adegun et al. [30] conducted a numerical investigation of normal convective heat transfer and fluid flow within a concentric square ring featuring an internal inclined elliptical cylinder subjected to isothermal heating and cooling, as illustrated in Figure 3. The researchers employed the Galerkin finite element method to solve the governing elliptic conservation equations. The parameters evaluated included Rayleigh numbers ranging from 10^3 to 10^3 and elliptical orientation angles varying from 0° to 90° . Additionally, an aspect ratio was considered, with values ranging from 1 to 3. This study provides insights into the effects of geometric configuration and thermal conditions on convective heat transfer characteristics.

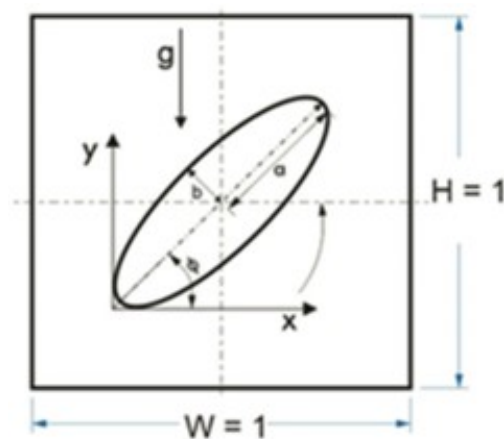


Figure 3. Physical coordinate geometry. [30]

Cho, Ha et al. [31] investigated two-dimensional natural convection numerically in a square container with a vertical arrangement of two elliptical cylinders. They used the Immersed Boundary Method (IBM), which combines the FVM and Immersed Boundary Method, to precisely depict the cylinders' virtual wall limits. There was a range of 0.25 to 4.00 for the elliptical cylinders' aspect ratio (AR) and 10^4 to 10^6 for their Rayleigh number (Ra). The study's main objective was to examine how the elliptical cylinders' varying aspect ratios affected the flow and heat fields.

Zhang et al. [32] focused on the numerical study of steady natural convection in a cold outer square enclosure containing a hot inner elliptical cylinder. They utilized the multiscale element-free Galerkin (VMEFG) method to conduct their numerical investigations. The study maintained a constant Prandtl number ($Pr = 0.71$) and an eccentricity of $\varepsilon = 0.9$ while examining different values of the dimensionless major axis ($a = 0.2, 0.3, 0.4$), the inclined angle of the outer square enclosure ($\gamma = 0^\circ, 15^\circ, 30^\circ, 45^\circ$), and the Rayleigh number ($Ra = 10^3, 10^4, 5 \times 10^4, 10^5, 10^6$). Their study's findings are shown in Figure 4, which highlights the intricate relationship between the system's thermal dynamics and geometric design.

Park et al. [33] considered two-dimensional natural convection numerically in a square enclosure with a vertical array of heated circular and elliptical cylinders, with Rayleigh numbers between $10^4 \leq Ra \leq 10^6$. Their study kept the Prandtl number constant at 0.7. The cylinder walls' borders were precisely captured by them using an immersed boundary approach. Their primary objective was to determine the impacts of the elliptical cylinder's inclination angle in this design statistically (Figure 5).

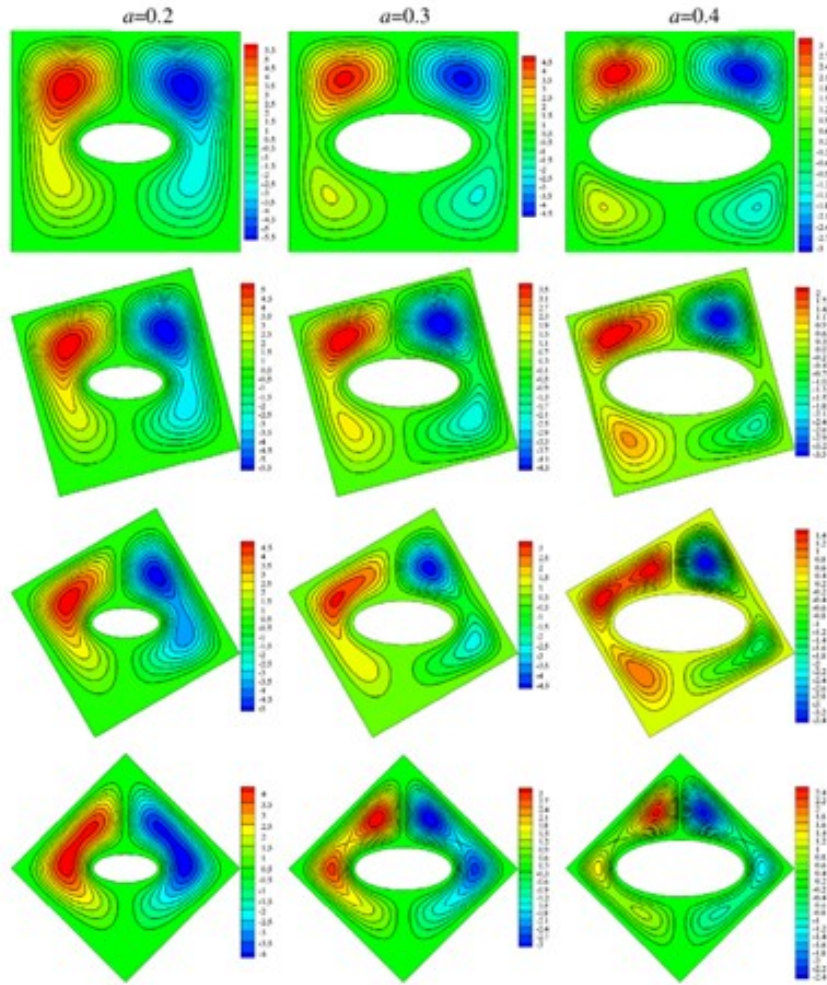


Figure 4. Streamlines for various a and γ values when $Ra = 5 \times 10^4$ [32]

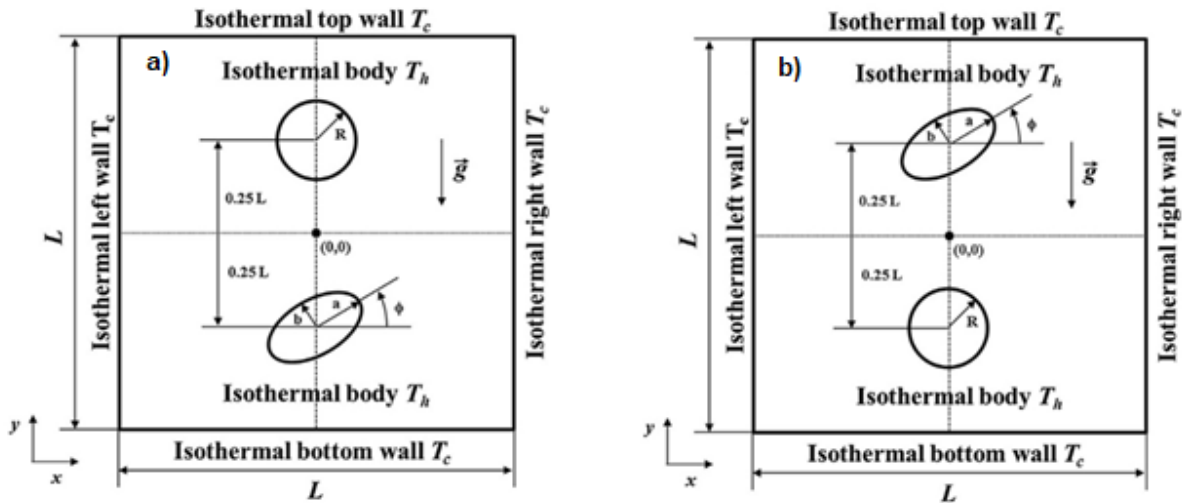


Figure 5. Physical model boundary conditions, coordinate system, and computational domain: (a) lower elliptical cylinder; (b) upper elliptical cylinder.[33]

Ibrahim et al. [34] studied natural convection inside cavities to introduce nanoparticles into the core fluid to improve heat transmission in various package forms. For their numerical computations, they used the COMSOL software, which is based on the Galerkin finite element method. The following parameters were used: the radius of the inner circle ($R = 0.15$), the radii of the inner elliptical cylinder ($R_x = 0.2$ and $R_y = 0.15$), the inclination angles ($-45^\circ, -30^\circ, 0^\circ, 30^\circ, 45^\circ$), the solid volume percent ($\phi = 0.05$), and the Rayleigh number Ra (varying from 10^3 to 10^6).

2.3.3 Inner circular body and cylinder

The magneto-hydrodynamic (MHD) heat transfer problem in a square open cavity containing a heated circular cylinder at the center has been investigated by Hossain et al. [35]. This study's objective is to explain how MHD affects flow and thermal fields when a heated circular cylinder is present, as visualized through graphical representations. They employed a numerical technique based on the weighted Galerkin residual method for finite element formulation. Heat transfer and fluid movement within the cavity depend on the Rayleigh number (Ra), Hartmann number (Ha), and heat flux (q). In this inquiry, the Prandtl number is fixed at $Pr = 0.72$ and the heat flow $q = 100$. The ranges for Ra and Ha are 10^3 to 10^4 and 0 to 400, respectively.

Shruti et al. [36] evaluated the combined effects of variations in Darcy and Rayleigh numbers on natural convection around two vertically arranged heated porous cylinders of different diameters in a square container. They employed the D_2Q_9 model to perform numerical simulations using a Boltzmann network. The following variations in flow and heat transmission were analyzed in relation to the Darcy and Rayleigh numbers and the cylinder volume: Porosity (ϵ) = 0.629, 0.977, and 0.993, that correspond to the related Darcy numbers; Rayleigh number (Ra) = 10^4 , 10^5 , and 10^6 ; and Darcy number (Da) = 10^{-6} , 10^{-4} , and 10^{-2} .

2.3.4 Inner cross shape

Ahmed and Aly [37] performed numerical simulations of natural convection induced by a hot cross-shaped body filled with stationary and moving solid particles. They utilized the improved incompressible particle hydrodynamics (ISPH) method to simulate the buoyancy-driven flow inside the enclosure. The key parameters in their investigation included the cross length L_{cross} (ranging from 0 to 0.8), solid particle depth L_{solid} (ranging from 0.02 to 1.8), time variations τ (ranging from 0.002 to 0.3), and the Rayleigh number Ra (ranging from 10^3 to 10^5). Their results indicated that the configuration with cold and moving solid particles resulted in the highest heat transfer rate, while the scenario with fixed and cold particles produced the lowest rate.

2.3.5. Square enclosure with two wavy sided walls

Ali et al. [38] conducted a numerical investigation of the flow and heat transfer components of buoyancy-driven convection in a hybrid cavity filled with nanofluids (Figure 6). The non-dimensional governing equations were solved using the finite element method. The simulation changed a variety of factors, such as the heater length (0.2 L to 0.6 L), the solid heat generation cylinder's radius (0.05 L to 0.2 L), the hybrid volume fraction (0% to 5%), the Rayleigh number (10^4 to 10^7), and the Hartmann number (0 to 50). With a constant Prandtl number of 6.2 and a thermal conductivity ratio of 5, the study found that increasing mesh configurations had minimal impact on the average Nusselt number, resulting in a satisfactory solution with 17,164 nodes and 33,554 elements (Figure 7).

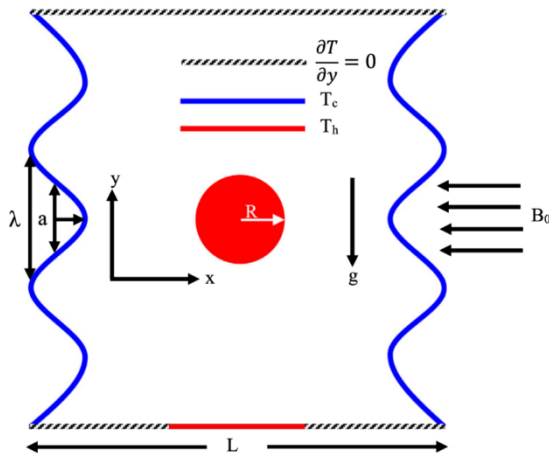


Figure 6. The current study's physical model. [38]

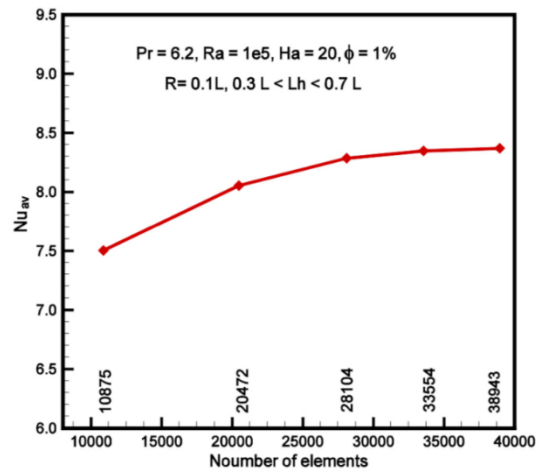
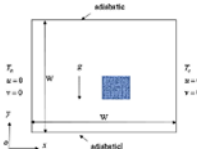
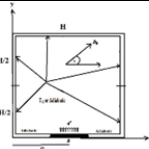
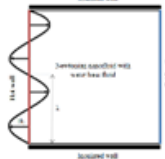
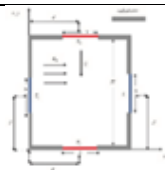
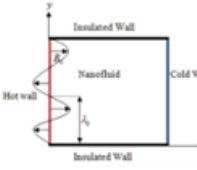
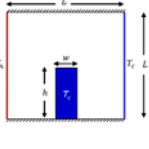
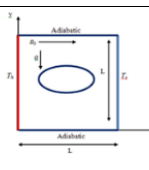
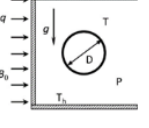
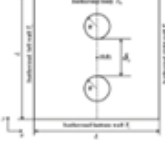


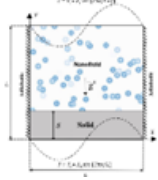
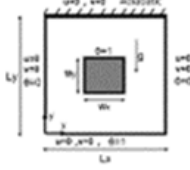
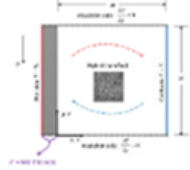
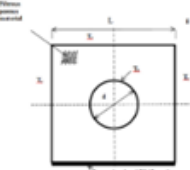
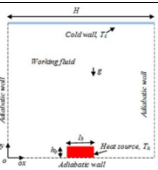
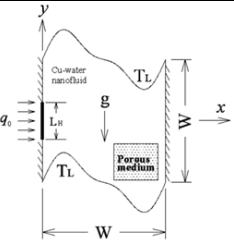
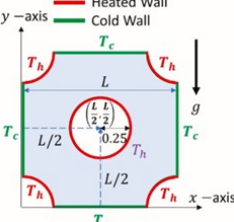
Figure 7. Grid refinement test. [38]

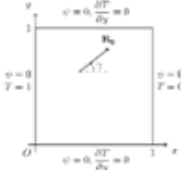
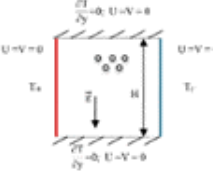
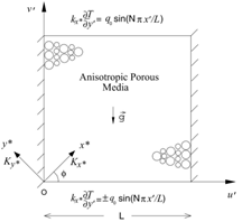
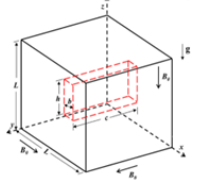
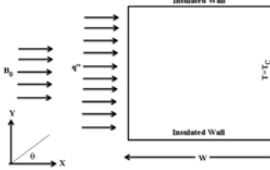
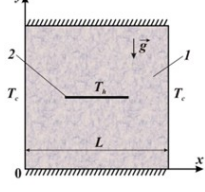
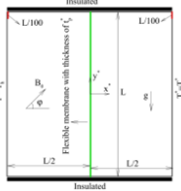
2.4. Triangular inside a square with MHD

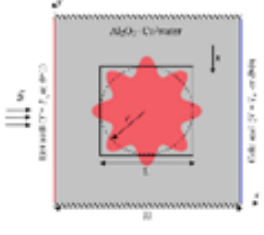
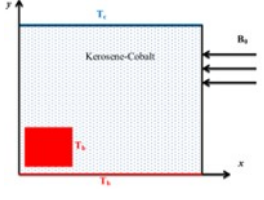
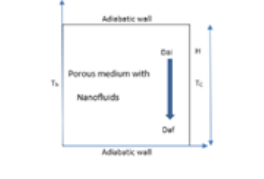
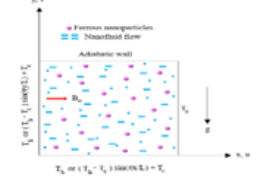
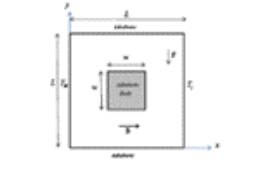
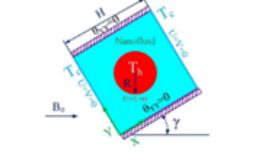
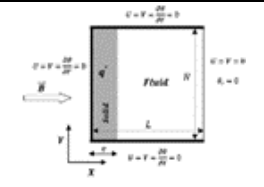
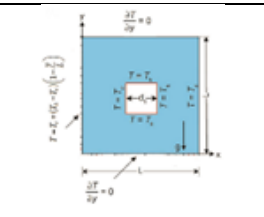
Vijaybabu and Dhinakaran [39] explored, using the Boltzmann method, the natural convection heat transfer between a cold square cavity and a hot, permeable triangular cylinder affected by a magnetic field. The study studied the effects of key parameters, specifically Rayleigh numbers ranging from 10^4 to 10^6 and Darcy numbers from 10^{-6} to 10^{-2} . For Hartmann numbers $Ha = 0, 25, \text{ and } 50$, the results are shown using streamlines, velocity profiles, isotherms, and local, surface, and mean Nusselt numbers. The results indicate that the high viscous resistance within the porous triangular cylinder at $Da = 10^{-6}$ effectively blocks fluid flow through it, regardless of Rayleigh or Hartmann values.

Table 1. A summary of the Effect of Different Internal and external bodies in Square Containers on Natural Convection

Reference	Major topic	Enclosure shape	Results
[14]	Natural convection in silver nanofluid		<ul style="list-style-type: none"> - Increasing H and y strengthens solid isotherms - Average Nusselt number increases.
[15]	MHD Natural convection		<ul style="list-style-type: none"> - Average Nusselt number increases with solid volume fraction.
[19]	MHD entropy generation in a ferrofluid		<ul style="list-style-type: none"> - Periodic magnetic field leads to higher total entropy than uniform field - Effect is consistent across Ha and λ values
[20]	MHD convection		<ul style="list-style-type: none"> - Fluid speed decreases significantly with increasing Hartmann number
[26]	MHD convection with nanofluid		<ul style="list-style-type: none"> - Heat transfer rate increases with magnetic field inclination angle (up to critical angle)
[28]	Natural convection with cold obstacle		<ul style="list-style-type: none"> - Heat transfer improves with increasing Rayleigh number, nanoparticle volume fraction, and cold mass height
[29]	MHD convection with elliptic shape		<ul style="list-style-type: none"> - Buoyant force increases with Rayleigh number
[35]	MHD free convection		<ul style="list-style-type: none"> - Heat flow decreases with increasing Hartmann number
[40]	Double inner cylinders		<ul style="list-style-type: none"> - Flow transitions from stable to unstable at Ra = 10⁶.

[41]	Nanofluid convection in porous media		- Stable natural convection behavior in inclined porous media
[42]	Conjugate natural convection		- Phase deviation significantly alters flow and temperature distribution
[43]	Hot obstacle convection		Nusselt number decreases on cold walls - Shape coefficient increases as surface ratio decreases
[44]	Hybrid nanofluid flow		- Local Nusselt number sharply drops from bottom to top of cavity
[45]	Heated cylinder convection		- Average Nusselt number increases with thermal conductivity ratio at specific Grashof numbers
[46]	Nanofluid with thermal source		- Nanoparticles <6% enhance heat transfer at high Ra and inclination angles <math><30^\circ</math>
[47]	Wavy surfaces		- Nu_m and Be increase while S_t decreases with increasing ϕ and aa_w .
[48]	Round barriers & curved corners		- Central temperature increases by 400% as barrier radius grows from 0.1 to 0.3

[49]	MHD convection under slope		<ul style="list-style-type: none"> - Stream function and vorticity decrease with Ha - Increase with Ra
[50]	Alumina nanofluid convection		<ul style="list-style-type: none"> - Heat transfer improves with higher solid volume fraction and Rayleigh number
[51]	Finned nanofluid cavity		<ul style="list-style-type: none"> - Heat transfer enhanced by increasing Rayleigh number, fin number, location, and length
[52]	Sinusoidal heating		<ul style="list-style-type: none"> - Flow strength decreases when $N > 1$
[53]	3D convection		<ul style="list-style-type: none"> - Vertical plates transfer heat more efficiently than horizontal plates across Ac and Ha
[54]	Entropy and inclination effects		<ul style="list-style-type: none"> - Nusselt number and entropy more sensitive to tilt angle (θ) than Hartmann number
[55]	Heated plate in porous cavity		<ul style="list-style-type: none"> - Higher radiation parameter, plate length, and Darcy number enhance heat transfer
[56]	MHD convection with flexible membrane		<ul style="list-style-type: none"> - Hartmann number changes affect heat transfer and membrane shape

<p>[57]</p>	<p>Hybrid nanofluid & wavy cylinder</p>		<ul style="list-style-type: none"> - Convective flow increases with Ra and conductivity - Decreases with Hartmann number and undulation effects
<p>[58]</p>	<p>Ferrofluid in porous cavity</p>		<ul style="list-style-type: none"> - Nusselt number increases with Darcy and Rayleigh numbers - Decreases with Hartmann number
<p>[59]</p>	<p>Nanofluid in porous cavity</p>		<ul style="list-style-type: none"> - Low permeability reduces flow and heat transfer - High permeability improves nanofluid mobility
<p>[60]</p>	<p>Uneven wall heating</p>		<ul style="list-style-type: none"> - Flow rate declines with higher nanoparticle concentration and Hartmann number
<p>[61]</p>	<p>MHD with adiabatic flow</p>		<ul style="list-style-type: none"> - Magnetic field significantly alters flow at high Prandtl and Hartmann numbers
<p>[62]</p>	<p>Inclined cavity with circular baffle</p>		<ul style="list-style-type: none"> - Heat transfer rate increases on right wall and decreases on left with increased inclination angle
<p>[63]</p>	<p>Uneven heat source with solid wall</p>		<ul style="list-style-type: none"> - Fluid flow strength rises with Ra_f regardless of k_f
<p>[64]</p>	<p>Heated cylinder</p>		<ul style="list-style-type: none"> - Right-wall local Nusselt number increases with Ra - Stronger eddies observed

2.5. Inner body studies without MHD

Cho et al. [40] conducted a numerical investigation into two-dimensional natural convection within a square container, examining various configurations of two internal cylinders at Rayleigh numbers ranging from $10^3 \leq Ra \leq 10^6$. Their simulations, based on the immersed boundary method, provided precise solutions. Results indicated that, at lower Rayleigh numbers, the solutions remained stable regardless of variations in δ . However, when the Rayleigh number increased to $Ra = 10^6$, the solutions became unstable for configurations with $\delta_h = 0.1L$, and $\delta_d = 0.2L$. Additionally, the average Nusselt number $\langle \overline{Nu_c} \rangle$ increased by approximately 29.2%, 12.8%, and 30.8% for the cases of δ_v , δ_h , and δ_d , respectively. Similarly, the average values of $\langle \overline{Nu_{En}} \rangle$ rose by around 27.7%, 12.4%, and 31.0% in these configurations.

Alsabery et al. [41] used a finite difference approach to study natural convection heat transport in an inclined square cavity with a porous layer and a nanofluid. The study concentrated on the effects of the following important parameters: cavity inclination angle ($0^\circ \leq \phi \leq 90^\circ$), phase deviation ($0 \leq \gamma \leq \pi$), amplitude ratio ($0 \leq \varepsilon \leq 1$), porous layer thickness ($0.1 \leq S \leq 0.9$), the Darcy number ($10^{-5} \leq Da \leq 10^{-3}$), and nanoparticle volume fraction ($0 \leq \phi \leq 0.2$). Rayleigh number ($Ra_{bf} = 10^4, 10^5$) and Prandtl number ($Pr_{bf} = 6.2$). Average Nusselt number values were computed for various ϕ and S values, revealing significant flow structure enhancement at lower inclination angles. The flow was observed as a cell in the nanofluid layer that rotates clockwise.

In another study, Alsabery [42] investigated conjugate natural convection in a square cavity including sinusoidal temperature fluctuations along the horizontal walls, focusing on a nanofluid devoid of an interior body. The study employed the finite difference method to investigate the effects of various parameters, including Rayleigh number ($10^5 \leq Ra \leq 10^8$), nanoparticle volume fractions ($0 \leq \phi \leq 0.2$), phase deviations ($0 \leq \gamma \leq \pi$), amplitude ratio ($0 \leq \varepsilon \leq 1$), wall-to-nanofluid thermal conductivity ratio ($0.44 \leq k_r \leq 23.8$), and wall thickness-to-height ratio ($0 \leq S \leq 0.7$).

Alturaihi et al. [44] explored natural convection within a heated cylinder located in a square cavity filled with a porous medium. Key parameters, including the Prandtl number ($Pr = 0.7$) and Darcy number ($Da = 0.01$), were selected for analysis. Five levels of porosity ($\varepsilon = 0.4, 0.5, 0.55, 0.6$ and 0.65) were considered, in addition to different values of the thermal conductivity ratio (kr) and Grashof number (Gr). Their findings revealed that increased porosity significantly enhances convective heat transfer within the cavity by strengthening fluid flow patterns. In a related study, Ghaleb et al. [45] numerically investigated Spontaneous natural convection in a square cavity containing a hybrid nanofluid of Ag, MgO, and water. They treated Rayleigh numbers between 10^3 and 10^5 and a nanoparticle volume percent between 0 and 0.02 with a fixed Prandtl number of $Pr = 6.2$ by solving the governing equations using the finite element method. According to their findings, hybrid nanofluids do not always improve the cavity's natural convection heat transmission.

El Mehdi et al. [46] studied the lattice Boltzmann flow behavior of a Cu/water nanofluid in a square cavity. Their simulations covered various Rayleigh numbers (from 10^5 to 0.5×10^7), cavity inclination angles (0° to 90°), and nanoparticle volume percentages (0 – 8%). The study assessed the effects of these parameters on fluid rheology and isothermal distributions within the cavity. Findings revealed that adding 8% nanoparticles effectively prevented flow separation.

Cho et al. [47] presented the natural convection of nanofluids in a porous cavity with wavy top and bottom surfaces and a vertical wall that is partially heated. They conducted numerical simulations to examine the effects of several parameters, including the irreversibility distribution (χ) divided by the Bejan number (Be), the length of the heated wall surface (L_H^*), the surface wavy amplitude (a_w), the Rayleigh number (Ra), the Darcy number (Da), the porosity (ϵ), and the nanoparticle volume fraction (ϕ). The average Nusselt number (Nu_m), energy flow vector distribution, and total entropy generation (S_t) were among the main topics of their investigation. Using the Tri-Diagonal Matrix Algorithm (TDMA), they were able to solve the governing systems.

2.6. Conventional Enclosure without inner body

Tezer-Sezgin et al. [49] surveyed natural convection in a square container containing hydrated aluminum oxide (Al_2O_3) when an external oblique magnetic field was present. This study employed two numerical techniques, specifically DRBEM, or Dual Reciprocity Boundary Element Method, and FEM, or Finite Element Method, utilizing different meshing types. The research focused on the effects of key flow parameters, including Rayleigh (Ra) and Hartmann (Ha) numbers, inclination angle (γ), and solid volume fraction (ϕ) are among them. Rayleigh and Hartmann numbers were as high as 10^7 and 300, respectively, for numerical simulations with inclination angles of $\gamma = 0, \pi/4, \pi/3,$ and $\pi/2$ with a solid volume fraction range of $0 \leq \phi \leq 0.20$. Notably, as illustrated in Figure 8, the DRBEM achieved mesh independence with 200 fixed boundary elements, while the FEM used 1152 quadratic triangular elements to ensure similar independence.

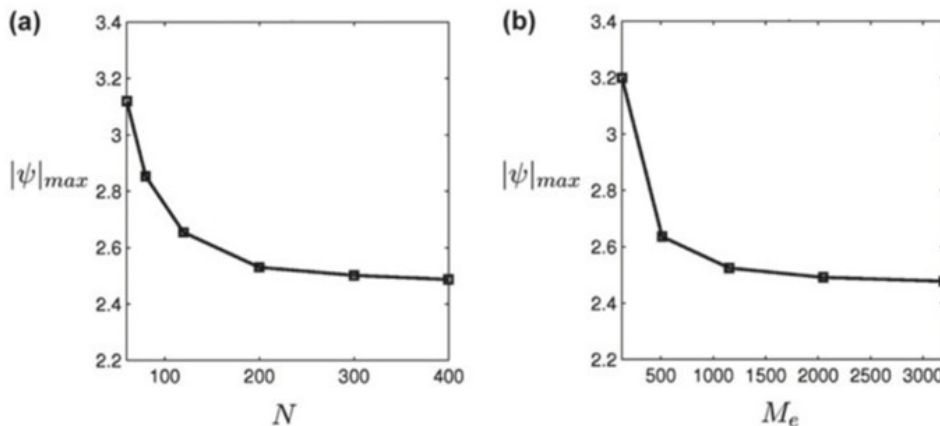


Figure 8. For Ha = 60, Ra = 10^5 , and $\phi = 0.03$ when $\gamma = 0$, the grid dependency is (a) DRBEM, (b) FEM.. [49]

Bouamoud and Houat [50] treated natural convection flow in two dimensions in a square hole with vertical walls that varied somewhat. Using a coupled population technique and the thermal grid Boltzmann method, they performed numerical simulations on a homogeneous nanofluid with alumina nanoparticles and pure water ($Pr = 6.2$) at solid volume fractions of $\phi = 0.02, 0.04, 0.06,$ and 0.08 in the laminar domain. According to their findings, the solid volume percentage of the nanoparticles has a major impact on the improvement of the heat transfer rate inside the cavity.

Chandra et al. [52] examined how different levels of polarization affected natural convection using the SIMPLER and Brinkman-extended-Darcy models, as well as the Alternating Direction Implicit (ADI) approach in certain situations. Eight non-dimensional parameters the Prandtl number (Pr), the Darcy number (Da), the Rayleigh number (Ra), the permeability ratio (K^*), the direction angle (ϕ), the thermal conductivity ratio (K^*), the periodicity parameter (N), and the porosity (ϵ) governed the velocity field and heat transfer rate, which they studied in relation to temperature.

Purusothaman et al. [53] investigated the finite volume method numerically for fluid flow and heat transfer in a cubic cavity caused by three-dimensional natural convection. Among the many parameters they calculated were the Hartmann number ($0 \leq H \leq 300$), the Prandtl number ($0.025 \leq Pr \leq 25$), and the plate's various aspect ratios ($AC = 0.5$ and 1.0). while keeping the Rayleigh number fixed at 10^7 . They concluded that both the heat transfer rate and the flow characteristics within the cavity are significantly influenced by the strength of the magnetic field for Prandtl numbers greater than or equal to 0.71 .

In another study, Mamourian et al. [54] investigated natural convection heat transfer and entropy generation in Al_2O_3 aqueous nanofluids within a square cavity subjected to an inclination angle and a constant axial magnetic field. They employed the governing equations are numerically solved using the finite volume approach. and utilized response surface methodology (RSM) for effective parameter analysis. The impacts of inclination angles ($0^\circ, 30^\circ,$ and 90°), Hartmann numbers ($0, 10, 30,$ and 50), and Rayleigh numbers ($10^3, 10^5,$ and 10^6) were investigated. At $\theta = 0.05$, they also investigated the effects of the inclination angle, Hartmann number, and Rayleigh number

Sivaraj and Sheremet [55] conducted A numerical simulation of thermal radiation and natural convection in a square porous cavity with a thin, isothermal heated plate sitting either vertically or horizontally in the middle. They solved the governing equations using an evenly layered grid structure and the finite volume approach. Their results showed that the radiation parameter, plate length, and Darcy number all considerably improve overall heat transmission in the cavity. A Rayleigh number of $Ra = 10^7$ was used to examine the effects of the radiation parameters ($0 \leq R_d \leq 2$), plate length ($0.25 \leq D \leq 0.75$), and Darcy number ($10^{-5} \leq Da \leq 10^{-2}$)

Mehryan et al. [56] numerically investigated unstable natural convection in a square cavity separated by an elastic membrane that is impermeable. They modeled the fluid-membrane interaction using the arbitrary Lagrangian-

Eulerian (ALE) technique in conjunction with the finite element method. Their study included a parametric analysis of key factors, including the Rayleigh number ($10^5 - 10^8$), Hartmann number (0 - 200), and magnetic field direction (0 - 180°). Their results indicated that the rotation of the fluid flow was enhanced with increasing magnetic field strength and directional adjustments.

2.7. inner body studies with MHD

Javed et al. [58] presented numerical results for free convection within a square container with a ferrofluid-saturated porous media inside, subjected to a constant magnetic field applied along the x-axis. They carried out numerical simulations using the finite element approach across a variety of flow parameters, such as the Rayleigh number, Hartmann number, Darcy number, and Prandtl number. Using constant values of $Pr = 6.2$, $Ra = 10^6$, $Ha = 30$, and nanoparticle volume fraction $\phi = 0.15$, their study specifically assessed the effects of the Darcy number on heat transmission and flow architectures at different blockage locations. They observed that as the Darcy parameter increases, the strength of clockwise rotation intensifies, as indicated by the maximum current function magnitude (ψ). Specifically, ψ values reached 0.09, 1.06, and 1.89 for $Da = 10^{-5}$, 10^{-4} , and 10^{-3} respectively, in the case of left boundary condition (LBC), while in the right boundary condition (RBC), they were 0.007, 0.08 and 1.9 for $Da = 10^{-5}$, 10^{-4} and 10^{-3} , respectively.

Sivaraj and Sheremet [65] considered natural convection within an inclined porous cavity containing a centrally placed, heat-conducting solid body, under the influence of a magnetic field oriented from various directions. They used a finite volume method on a uniformly meshed grid to solve the coupled partial differential equations governing fluid flow and heat transfer. The study focused on the effects of Hartmann number ($0 \leq Ha \leq 50$), cavity inclination angle ($-45^\circ \leq \xi \leq 90^\circ$), and magnetic field inclination angle ($0^\circ \leq \gamma \leq 180^\circ$) on flow properties, isotherms, and the average Nusselt number. Results showed that the average Nusselt number peaks at a cavity inclination of $\xi = 30^\circ$ without a magnetic field, while in the presence of a magnetic field ($Ha = 50$), it reaches its maximum at $\xi = 45^\circ$.

2.8. Previous studies without inner body and Without MHD

Cherifa et al. [59] treated the Galerkin finite element method was used to solve the dimensionless equations and the Buongiorno model was used to study laminar natural convection in a porous square cavity filled with nanofluids. They analyzed various parameters with a cavity height of $H = 2m$, a Prandtl number of 5.82, Rayleigh number of 10^5 , Darcy number of 10^{-2} , Lewis number of 1, and Brownian motion, thermophoresis, and buoyant force ratios all set to 0.1 ($N_r = N_b = N_t = 0.1$). Further investigations were performed across ranges of Rayleigh ($10^4 \leq Ra \leq 10^6$), Darcy ($10^{-5} \leq Da \leq 10^{-2}$), and an initial Darcy number that decreased to a final Darcy number of 10^{-5} .

Acharya et al. [60] explored the hydrothermal behavior of radiative aqueous nanofluid Fe_3O_4 within a square chamber. They employed the Galerkin finite element technique after transforming the main dimensional equations

into dimensionless form using similarity variables. Their simulations checked the impacts of the following fixed values: $Ra=10^4$, $Ha = 5$, $N = 0.5$, $\phi = 0.02$, $Pr = 6.2$, thermal radiation ($0.5 \leq N \leq 1.5$), Rayleigh number ($10^3 \leq Ra \leq 10^5$), and Hartmann number ($5 \leq Ha \leq 25$).

Scott et al. [66] studied the impact of various volume concentrations of AL_2O_3 -MWCNT (10:90) water-based hybrid nanofluids on heat transfer performance within a square cavity. Their findings indicated that hybrid nanofluids considerably outperformed single-nanoparticle nanofluids, with a maximum enhancement of 43.78% in heat transfer efficiency (h_{av}) at a concentration of 0.10 vol% at 50°C compared to deionized (DI) water. As Rayleigh numbers increased, the average Nusselt number (Nu_{av}) increased as well. for AL_2O_3 -MWCNT hybrid samples across different concentrations and base fluids, highlighting hybrid nanofluids' potential as effective heat transfer fluids.

3. Conclusion

This review presents a comprehensive overview of recent studies on natural convection heat transfer (NCHT) within square enclosures, both with and without the presence of internal bodies, and examines the influence of magnetic fields on fluid flow and thermal performance. Covering research conducted between 2015 and 2024, the review highlights key advancements as well as gaps in current knowledge, emphasizing areas where further investigation could significantly advance the field.

The analysis identifies several promising directions for future research:

- While circular internal bodies have been extensively examined, elliptical geometries remain underexplored. Further studies in this area may uncover distinctive thermal behaviors arising from their unique flow patterns.
- Most existing literature focuses on single-body configurations, or occasionally, systems with two or four bodies. Extending this research to include multi-body arrangements could improve understanding of complex thermal interactions and contribute to optimized enclosure designs for enhanced heat transfer.
- Future investigations should consider how varying magnetic field strengths and orientations interact with different internal body shapes, as this may provide new strategies for enhancing or controlling heat transfer.
- Unconventional geometries, such as pentagonal and hexagonal bodies, have the potential to significantly influence fluid dynamics and heat distribution. Exploring these shapes may reveal novel approaches for maximizing heat transfer within enclosures.

In summary, although substantial progress has been made in understanding NCHT in square enclosures, the outlined research directions are critical for further advancing theoretical models and practical

applications. Continued exploration in these areas will enable more precise control over heat transfer processes, particularly in systems influenced by internal geometries and magnetic fields, and will contribute meaningfully to both engineering and environmental technologies.

References

- [1] Tasnim, S., A. Mitra, H. Saha, M.Q. Islam, and S. Saha, MHD conjugate natural convection and entropy generation of a nanofluid filled square enclosure with multiple heat-generating elements in the presence of Joule heating. *Results in Engineering*, 17 (2023) :100993.
- [2] Wang, X.-Q. and A.S. Mujumdar, A review on nanofluids-part I: theoretical and numerical investigations. *Brazilian journal of chemical engineering*, 25 (2008) 613-630.
- [3] Kasaeian, A., R. Daneshzarian, O. Mahian, L. Kolsi, A.J. Chamkha, S. Wongwises, and I. Pop, Nanofluid flow and heat transfer in porous media: a review of the latest developments. *International Journal of Heat and Mass Transfer*, 107 (2017) 778-791.
- [4] Das, D., M. Roy, and T. Basak, Studies on natural convection within enclosures of various (non-square) shapes—A review. *International Journal of Heat and Mass Transfer*, 106 (2017) 356-406.
- [5] Biswal, P. and T. Basak, Entropy generation vs energy efficiency for natural convection based energy flow in enclosures and various applications: a review. *Renewable and Sustainable Energy Reviews*, 80 (2017) 1412-1457.
- [6] Sadeghi, M.S., N. Anadalikhah, R. Ghasemiasl, T. Armaghani, A.S. Dogonchi, A.J. Chamkha, H. Ali, and A. Asadi, On the natural convection of nanofluids in diverse shapes of enclosures: an exhaustive review. *Journal of Thermal Analysis and Calorimetry*, (2020) 1-22.
- [7] Giwa, S., M. Sharifpur, M. Ahmadi, and J. Meyer, A review of magnetic field influence on natural convection heat transfer performance of nanofluids in square cavities. *Journal of Thermal Analysis and Calorimetry*, 145 (2021) 2581-2623.
- [8] Hemmat Esfe, M., M. Afrand, and S. Esfandeh, Investigation of the effects of various parameters on the natural convection of nanofluids in various cavities exposed to magnetic fields: a comprehensive review. *Journal of Thermal Analysis and Calorimetry*, 140 (2020) 2055-2075.
- [9] Chen, S., W. Gong, and Y. Yan, Conjugate natural convection heat transfer in an open-ended square cavity partially filled with porous media. *International Journal of Heat and Mass Transfer*, 201 :124 .8p. 368-380.
- [10] Belhaj, S. and B. Ben-Beya, Numerical simulation of unsteady MHD natural convection of CNT-water nanofluid in square cavity heated sinusoidally from below. *Particulate Science and Technology*, 37(7) (2019) 851-870.
- [11] Joshi, P.S. and A. Pattamatta, Enhancement of natural convection heat transfer in a square cavity using MWCNT/Water nanofluid: an experimental study. *Heat and Mass Transfer*, 54 (2018) 2295-2303.
- [12] Hidayathulla Khan, B.M., K. Venkatadri, O. Anwar Bég, V. Ramachandra Prasad, and B. Mallikarjuna, Natural convection in a square cavity with uniformly heated and/or insulated walls using Marker-and-Cell Method. *International Journal of Applied and Computational Mathematics*, 4 (2018) 1-18.
- [13] Khatamifar, M., W. Lin, and L. Dong, Transient conjugate natural convection heat transfer in a differentially-heated square cavity with a partition of finite thickness and thermal conductivity. *Case Studies in Thermal Engineering*, 25 (2021) 100952.
- [14] Kumar, R., A. Bhattacharyya, and G. Seth, Heat transfer analysis on unsteady natural convection flow of silver nanofluid in a porous square cavity using local thermal non-equilibrium model. *Indian Journal of Physics*, (2021). 1-14.
- [15] Mansour, M. and M. Bakier, Influence of thermal boundary conditions on MHD natural convection in square enclosure using Cu–water nanofluid. *Energy Reports*, 1 (2015) 134-144.
- [16] Ben Hamida, M. and K. Charrada, Natural convection heat transfer in an enclosure filled with an ethylene glycol—copper nanofluid under magnetic fields. *Numerical Heat Transfer, Part A: Applications*, 67(8) (2015) 902-920.
- [17] Sreedevi, P. and P.S. Reddy, Effect of magnetic field and thermal radiation on natural convection in a square cavity filled with TiO₂ nanoparticles using Tiwari-Das nanofluid model. *Alexandria Engineering Journal*, 61(2) (2022)1541-1529
- [18] Haritha, C., B.C. Shekar, and N. Kishan, MHD natural convection heat transfer in a porous square cavity filled by nanofluids with viscous dissipation. *J. Nanofluids*, 7(5) (2018) 928-938.
- [19] Mehryan, S., M. Izadi, A.J. Chamkha, and M.A. Sheremet, Natural convection and entropy generation of a ferrofluid in a square enclosure under the effect of a horizontal periodic magnetic field. *Journal of Molecular Liquids*, 263 (2018) 510-525.
- [20] Mansour, M., S. Siddiqa, R.S.R. Gorla, and A. Rashad, Effects of heat source and sink on entropy generation and MHD natural convection of Al₂O₃-Cu/water hybrid nanofluid filled with square porous cavity. *Thermal Science and Engineering Progress*, 6 (2018) 57-71.

- [21] Al Kalbani, K.S., M.M. Rahman, S. Alam, N. Al-Salti, and I.A. Eltayeb, Buoyancy induced heat transfer flow inside a tilted square enclosure filled with nanofluids in the presence of oriented magnetic field. *Heat Transfer Engineering*, 39(6) (2018) 511-525.
- [22] Mahapatra, T. and R. Parveen, Entropy generation in MHD natural convection within curved enclosure filled with Cu-water nanofluid. *Journal of Nanofluids*, 8(5) (2019)1051-1065.
- [23] Uddin, M., S. Rasel, M. Rahman, and K. Vajravelu, Natural convective heat transfer in a nanofluid-filled square vessel having a wavy upper surface in the presence of a magnetic field. *Thermal Science and Engineering Progress*, 19 (2020) 100660.
- [24] Rajarathinam, M. and A. Chamkha, Effect of partial open on natural convection heat transfer of CNT–water nanofluid in a square cavity with magnetic field. *The European Physical Journal Plus*, 136(1) (2021) 52.
- [25] Devi, T.S., C.V. Lakshmi, K. Venkatadri, and M.S. Reddy, Influence of external magnetic wire on natural convection of non-Newtonian fluid in a square cavity. *Partial Differential Equations in Applied Mathematics*, 4 (2021) 100041.
- [26] Nishad, S., S. Jain, and R. Bhargava, Numerical simulation of natural convection within wavy square enclosure filled with nanofluid under magnetic field using EFGM with parallel algorithm. *International Journal of Numerical Methods for Heat & Fluid Flow*, 31(12) (2021) 3505-3526.
- [27] Munshi, M.J.H., A. Bhuiyan, and M. Alim, A numerical study of natural convection in a square enclosure with non-uniformly heated bottom wall and square shape heated block. *Am. J. Eng. Res.(AJER)*,4(5) (2015) 124-137.
- [28] Boulahia, Z., A. Wakif, and R. Sehaqui, Natural convection heat transfer of the nanofluids in a square enclosure with an inside cold obstacle. *International journal of innovation and scientific research*, 21(2) (2016) 367-375.
- [29] Munshi, M.J.H., M .Alim, A. Bhuiyan, and G. Mostafa, Effect of a Magneto-hydrodynamic Natural Convection in a Square Cavity with Elliptic Shape Adiabatic Block. *American Journal of Engineering Research*, 4 (2015) 10-22.
- [30] Adegun, I., S. Ibitoye, and A. Bala, Effect of selected geometric parameters on natural convection in concentric square annulus. *Australian Journal of Mechanical Engineering*, 20(4) (2022) 1142-1153.
- [31] Cho, H.W., M.Y. Ha, and Y.G. Park, Natural convection in a square enclosure with two hot inner cylinders, Part II: The effect of two elliptical cylinders with various aspect ratios in a vertical array. *International Journal of Heat and Mass Transfer*, 135 (2019) 962-973.
- [32] Zhang, P., X. Zhang, J. Deng, and L. Song, A numerical study of natural convection in an inclined square enclosure with an elliptic cylinder using variational multiscale element free Galerkin method. *International Journal of Heat and Mass Transfer*, 99 (2016) 721-737.
- [33] Park, S.H., Y.M. Seo, M.Y. Ha, and Y.G. Park ,Natural convection in a square enclosure with different positions and inclination angles of an elliptical cylinder Part I: A vertical array of one elliptical cylinder and one circular cylinder. *International Journal of Heat and Mass Transfer*, 126 (2018) 173-183.
- [34] Ibrahim, M.N.J., K.A. Hammoodi, A.D. Abdulsahib, and M.A. Flayyih, Study of natural convection inside inclined nanofluid cavity with hot inner bodies (circular and ellipse cylinders). *International Journal of Heat and Technology*, 40(3) (2022) 699-705.
- [35] Hossain, S.A., M. Alim, and S. Saha, A finite element analysis on MHD free convection flow in open square cavity containing heated circular cylinder. *American Journal of Computational Mathematics*, 5(01) (2015) 41-54.
- [36] Shruti, B., M.M. Alam, A. Parkash, and S. Dhinakaran, Darcy number influence on natural convection around porous cylinders in an enclosure using Darcy-Brinkman-Forchheimer model: LBM study. *Case Studies in Thermal Engineering*, 45 (2023) 102907.
- [37] Ahmed, S.E. and A.M. Aly, Natural convection in a nanofluid-filled cavity with solid particles in an inner cross shape using ISPH method. *International Journal of Heat and Mass Transfer*, 141 (2019) 390-406.
- [38] Ali, M.M., R. Akhter, and M. Alim, Hydromagnetic natural convection in a wavy-walled enclosure equipped with hybrid nanofluid and heat generating cylinder. *Alexandria Engineering Journal*, 60(6) (2021) 5245-5264.
- [39] Vijaybabu, T. and S. Dhinakaran, MHD Natural convection around a permeable triangular cylinder inside a square enclosure filled with Al₂O₃– H₂O nanofluid: An LBM study. *International Journal of Mechanical Sciences*, 153 (2019) 500-516.
- [40] Cho, H.W., Y.M. Seo, G.S. Mun, M.Y. Ha, and Y.G. Park, The effect of instability flow for two-dimensional natural convection in a square enclosure with different arrays of two inner cylinders. *International Journal of Heat and Mass Transfer*, 114 (2017) 307-317.
- [41] Alsabery, A., A. Chamkha, H. Saleh, and I. Hashim, Natural convection flow of a nanofluid in an inclined square enclosure partially filled with a porous medium. *Scientific reports*, 7(1) (2017) 2357.
- [42] Alsabery, A., A. Chamkha, H. Saleh, and I. Hashim, Heatline visualization of conjugate natural convection in a square cavity filled with nanofluid with sinusoidal temperature variations on both horizontal walls. *International Journal of Heat and Mass Transfer*, 100 (2016) 835-850.
- [43] Rahmati, A. and A. Tahery, Numerical study of nanofluid natural convection in a square cavity with a hot obstacle using lattice Boltzmann method. *Alexandria engineering journal*, 57(3) (2018) 1271-1286.

- [44] Alturaihi, M.H., L. Jassim, A.R. ALguboori, L.J. Habeeb, and H.K. Jalghaf, Porosity influence on natural convection heat transfer from a heated cylinder in a square porous enclosure. *Journal of Mechanical Engineering Research and Developments*, 43(6) (2020) 236-254.
- [45] Ghalambaz, M., A. Doostani, E. Izadpanahi, and A.J. Chamkha, Conjugate natural convection flow of Ag–MgO/water hybrid nanofluid in a square cavity. *Journal of Thermal Analysis and Calorimetry*, 139(3) (2020) 2321-2336.
- [46] El Mehdi, B., Lattice Boltzmann Computations of Natural Convection Heat Transfer of Nanofluid in a Square Cavity Heated by Protruding Heat Source. *Journal of Thermal Science and Engineering Applications*, 20 (2020) 001000-1.
- [47] Cho, C.-C., Effects of porous medium and wavy surface on heat transfer and entropy generation of Cu-water nanofluid natural convection in square cavity containing partially-heated surface. *International Communications in Heat and Mass Transfer*, 119 (2020) 104925.
- [48] Hamid, M., M. Usman, W.A. Khan, R.U. Haq, and Z. Tian, Characterizing natural convection and thermal behavior in a square cavity with curvilinear corners and central circular obstacles. *Applied Thermal Engineering*, 248 (2024) 123133.
- [49] Tezer-Sezgin, M., C. Bozkaya, and Ö. Türk, Natural convection flow of a nanofluid in an enclosure under an inclined uniform magnetic field. *European Journal of Computational Mechanics*, 25(1-2) (2016) 2-23.
- [50] Bouamoud, B. and S. Houat, Mesoscopic study of natural convection in a square cavity filled with alumina-based nanofluid. *Energy Procedia*. 139 (2017) 758-765.
- [51] Arjun, K. and K. Rakesh, MHD natural convection heat transfer in a nanofluid filled finned square cavity. *Journal of Mechanical Engineering Research & Developments*, 40 (2017) 481-489.
- [52] Chandra, H., P. Bera, and A.K. Sharma, Natural convection in a square cavity filled with an anisotropic porous medium due to sinusoidal heat flux on horizontal walls. *Numerical Heat Transfer, Part A: Applications*, 77(3) (2020) 317-341.
- [53] Purusothaman, A., H. Oztop, N. Nithyadevi, and N.H. Abu-Hamdeh, 3D natural convection in a cubical cavity with a thermally active heater under the presence of an external magnetic field. *Computers & Fluids*, 128 (2016) 30-40.
- [54] Mamourian, M., K.M. Shirvan, and I. Pop, Sensitivity analysis for MHD effects and inclination angles on natural convection heat transfer and entropy generation of Al₂O₃-water nanofluid in square cavity by Response Surface Methodology. *International Communications in Heat and Mass Transfer*, 79 (2016) 46-57.
- [55] Sivaraj, C. and M.A. Sheremet, Natural convection coupled with thermal radiation in a square porous cavity having a heated plate inside. *Transport in Porous Media*, 114(2016) 843-857.
- [56] Mehryan, S., M. Ghalambaz, M.A. Ismael, and A.J. Chamkha, Analysis of fluid-solid interaction in MHD natural convection in a square cavity equally partitioned by a vertical flexible membrane. *Journal of Magnetism and Magnetic Materials*, 424 (2017) 161-173.
- [57] Tayebi, T. and A.J. Chamkha, Effects of various configurations of an inserted corrugated conductive cylinder on MHD natural convection in a hybrid nanofluid-filled square domain. *Journal of Thermal Analysis and Calorimetry*, 143(2) (2021) 1399-1411.
- [58] Javed, T., Z. Mehmood, and Z. Abbas, Natural convection in square cavity filled with ferrofluid saturated porous medium in the presence of uniform magnetic field. *Physica B: condensed matter*, 506 (2017) 122-132.
- [59] Cherifa, B., B. Mohamed, M. Abderrahim, and K. Fatima-Zohra, Unsteady natural convection in a porous square cavity saturated by nanofluid using buongiorno model: variable permeability effect on homogeneous porous medium. *CFD Letters*, 14(7) (2022) 42-61.
- [60] Acharya, N., Finite element analysis on the hydrothermal pattern of radiative natural convective nanofluid flow inside a square enclosure having nonuniform heated walls. *Heat Transfer*, 51(1) (2022) 323-354.
- [61] Hussein, A.K., H. Ashorynejad, S. Sivasankaran, L. Kolsi, M. Shikholeslami, and I. Adegun, Modeling of MHD natural convection in a square enclosure having an adiabatic square shaped body using Lattice Boltzmann Method. *Alexandria Engineering Journal*, 55(1) (2016) 203-214.
- [62] Li, Z., A.K. Hussein, O. Younis, M. Afrand, and S. Feng, Natural convection and entropy generation of a nanofluid around a circular baffle inside an inclined square cavity under thermal radiation and magnetic field effects. *International Communications in Heat and Mass Transfer*, 116 (2020) 104650.
- [63] Bouchair, R., A. Bourouis, and A. Omara, Conjugate MHD natural convection in a square cavity with a non-uniform heat source thick solid partition. *International Journal for Computational Methods in Engineering Science and Mechanics*, (5)23 (2022) 396-411.
- [64] Sivarami Reddy, C., V. Ramachandra Prasad, and K. Jayalakshmi, Numerical simulation of natural convection heat transfer from a heated square cylinder in a square cavity filled with micropolar fluid. *Heat Transfer*, (6)50(2021:) 5267-5285.
- [65] Sivaraj, C. and M.A. Sheremet, MHD natural convection in an inclined square porous cavity with a heat conducting solid block. *Journal of Magnetism and Magnetic materials*, 426 (2017) 351-360.
- [66] Scott, T.O., D.R. Ewim, and A.C. Eloka-Eboka, Experimental investigation of natural convection Al₂O₃-MWCNT/water hybrid nanofluids inside a square cavity. *Experimental Heat Transfer*, 37(3) (2024) 294-312.



Thermodynamic and Mechanistic Insights into Paracetamol Removal from Aqueous Solutions by Graphitic Carbon Nitride Nanosheets

Ayyob M. Bakry¹, Abdulmajeed M. Jabbari², Zeinhom H. Mohamed¹, Mohammed B. Hawsawi³,
Nasser Amri¹ and R E Azooz^{1,*}

¹ Department of Physical Sciences, Chemistry Division, College of Science, Jazan University, P.O. Box. 114, Jazan 45142, Kingdom of Saudi Arabia.

² Department of Pharmaceutical Chemistry, College of Pharmacy, University of Hail, 81442, Hail, Saudi Arabia

³ Department of Chemistry, Faculty of Science, Umm Al-Qura University, Makkah 21955, Saudi Arabia

*Corresponding author: (R E Azooz), *Email Address:* rramadan@jazanu.edu.sa

Abstract

This study explored the potential of raw graphitic carbon nitride (g-C₃N₄) as a low-cost adsorbent for removing paracetamol from water. The material's structure and properties were analyzed using various techniques, including X-ray diffraction (XRD), Fourier-transform infrared spectroscopy (FTIR), Ultraviolet visible (UV-Vis) spectroscopy, and Transmission electron microscopy (TEM). Factors affecting paracetamol adsorption, such as pH, contact time, adsorbent dosage, and initial paracetamol concentration, were investigated. The results showed that a maximum adsorption capacity of 1.1 mg/g was achieved at 25 °C within 60 minutes. Both Langmuir and pseudo-second-order models accurately described the adsorption behavior. Density functional theory (DFT) confirms the stability of the complex formed between Paracetamol and Graphitic carbon nitride (g-C₃N₄), and Molecular dynamics (MD) and FTIR confirm the stability of H-bond formation a high adsorption energy of -38.640×10^{-3} kcal/mol. These findings suggest that modified graphitic carbon nitride can be a promising, eco-friendly, and affordable adsorbent for removing pharmaceutical contaminants from water.

Keywords: Paracetamol, Adsorption, g-C₃N₄, DFT, MD, Adsorption energy, and Removal.

<https://doi.org/10.63070/jesc.2025.002>

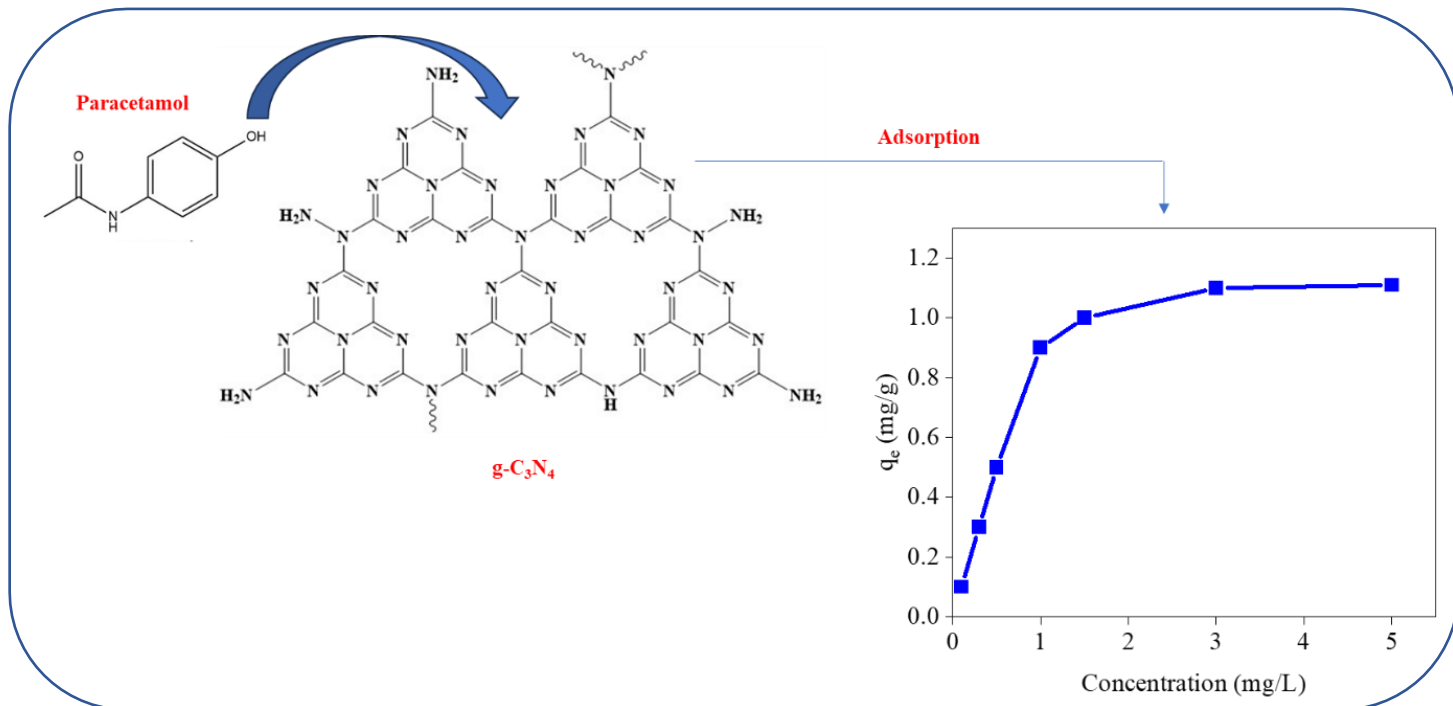
Received 09 February 2025; Revised 25 April 2025; Accepted 08 May 2025.

Available online 16 May 2025.

Published by Islamic University of Madinah on behalf of *Islamic University Journal of Applied Sciences*. This is a free open access article.

Graphical Abstract

TOF



1. Introduction

Pharmaceutical water contamination is a global concern due to the widespread use of pharmaceuticals and their potential to pollute water sources. These contaminants can enter water bodies through various pathways, including wastewater discharges, improper disposal, and agricultural runoff. The presence of pharmaceuticals in water can have adverse effects on aquatic ecosystems, human health, and the environment.[1, 2] Pharmaceuticals can disrupt the hormonal balance of aquatic organisms, leading to reproductive issues and developmental abnormalities. In humans, exposure to contaminated water can have long-term health consequences, such as antibiotic resistance and endocrine disruption. Addressing pharmaceutical water contamination requires a multi-faceted approach, including improved wastewater treatment, proper medication disposal practices, and the development of sustainable pharmaceutical manufacturing processes.[2, 3] Among these contaminants, paracetamol is particularly concerning due to its frequent detection in water and wastewater. While concentrations may seem low, higher levels have been found in waste effluents, highlighting the need for effective removal methods to mitigate these environmental impacts.[4, 5]

Numerous techniques, such as photodegradation, membrane filtration, and ozonation, have been utilized for wastewater treatment.[5, 6] However, adsorption has emerged as a preferred method due to its simplicity, effectiveness, and environmental friendliness. This process involves the capture of pollutants onto the surface of an adsorbent material. One of the key advantages of adsorption is its versatility. Adsorbents can be modified to selectively target specific contaminants, like paracetamol, even in the presence of other molecules. This makes it particularly suitable for industrial wastewater treatment. Furthermore, adsorbed paracetamol can often be regenerated using appropriate eluents, allowing for the reuse of the adsorbent and reducing waste generation.[7, 8] A variety of materials have been explored for paracetamol adsorption, including activated carbon,[9] nitrogen-doped porous carbons,[10] and various frameworks.[11] The choice of adsorbent depends on factors like the specific properties of paracetamol and the desired water quality.

g-C₃N₄ is a promising alternative to activated carbon for adsorption applications. Unlike activated carbon, which is expensive and difficult to regenerate, g-C₃N₄ offers a more cost-effective and sustainable solution. This two-dimensional polymer boasts a honeycomb structure similar to graphene, composed of carbon and nitrogen atoms arranged in a triazine ring unit. This unique structure provides exceptional thermal and chemical stability, as well as a high surface area. The layered structure and abundant surface area of g-C₃N₄ create numerous binding sites for various molecules, making it an effective adsorbent. Moreover, the high nitrogen content of g-C₃N₄ enables strong interactions with pollutants, particularly those containing polar functional groups.[12-14] This combination of factors positions g-C₃N₄ as a promising adsorbent for a wide range of contaminants, including dyes, heavy metals, and organic pollutants from wastewater and air.

This study aimed to investigate the effectiveness of g-C₃N₄ as an adsorbent for removing paracetamol from aqueous solutions. Various experimental parameters were evaluated to optimize the adsorption process, including pH (2-12), concentration (0.1-5 ppm), temperature (25-50 °C), and contact time (5-480

min). Kinetic, isothermal, and thermodynamic analyses were conducted to gain a comprehensive understanding of the adsorption mechanism and equilibrium. Additionally, spectroscopic, DFT calculations and MD simulation were employed to explore the interaction between paracetamol and g-C₃N₄ during adsorption.

2. Experimental Section

2.1. Chemicals: All chemicals employed in this investigation were commercially accessible and exhibited high purity. Melamine (99.8%), sodium hydroxide (99%), hydrochloric acid (37%), methanol (99.5%), isopropanol (99.5%), ethanol (99.5%), and paracetamol (99.9%) were utilized. Deionized water (DIW) was the solvent for preparing the Paracetamol stock solution.

2.2. Synthesis of SNP-g-C₃N₄: Bulk g-C₃N₄ was synthesized by heating 10 grams of melamine in a ceramic crucible at 520°C for 4 hours in a digital furnace, using a heating rate of 5°C per minute. To produce g-C₃N₄ nanosheets, 100 milligrams of bulk g-C₃N₄ were dispersed in 1000 milliliters of a 3:1 isopropanol-to-water mixture. The suspension was then sonicated for 24 hours at room temperature. After centrifugation and washing with deionized water (3 times) and ethanol (1 time), the nanosheets were dried in an oven at 100°C for 6 hours.

2.3. Preparations of paracetamol solutions: 0.2 grams of paracetamol were precisely weighed and dissolved in 200 milliliters of DDW. The solution was then sonicated for 30 minutes to ensure complete dissolution and homogeneity. This stock solution was subsequently used to prepare solutions of varying concentrations (0.1, 0.3, 0.5, 1, 1.5, 3, and 5 ppm) in 100-milliliter volumetric flasks using DIW. A UV-visible spectrophotometer was employed to determine the concentration profile of paracetamol at its maximum absorbance wavelength (λ_{max}) of 249 nanometers.

2.4. Adsorption Optimization and Analysis: To determine optimal adsorption conditions, a series of experiments were conducted using a one-factor-at-a-time approach. Variables explored included pH (2-12), g-C₃N₄ dose (10 mg /10 mL), contact time (5-180 minutes), and temperature (25-50 °C). Drug solutions were prepared in separate glass flasks and incubated with the desired adsorbent dose. After reaching equilibrium, the solutions were centrifuged and filtered before analysis. The adsorption capacity (q_e), and adsorption efficiency (% R_e) were calculated using **Equations (1, and 2)**. To identify the rate-limiting step, kinetic studies were conducted. The adsorption rate of paracetamol was determined by quantifying the adsorbed amount at varying time intervals (q_t). **Equation (3)** was used for this calculation.

$$q_e = \frac{(C_0 - C_e)}{C_0} \times \frac{V}{W} \quad (1)$$

$$\%R_e = \frac{(C_0 - C_e)}{C_0} \times 100 \quad (2)$$

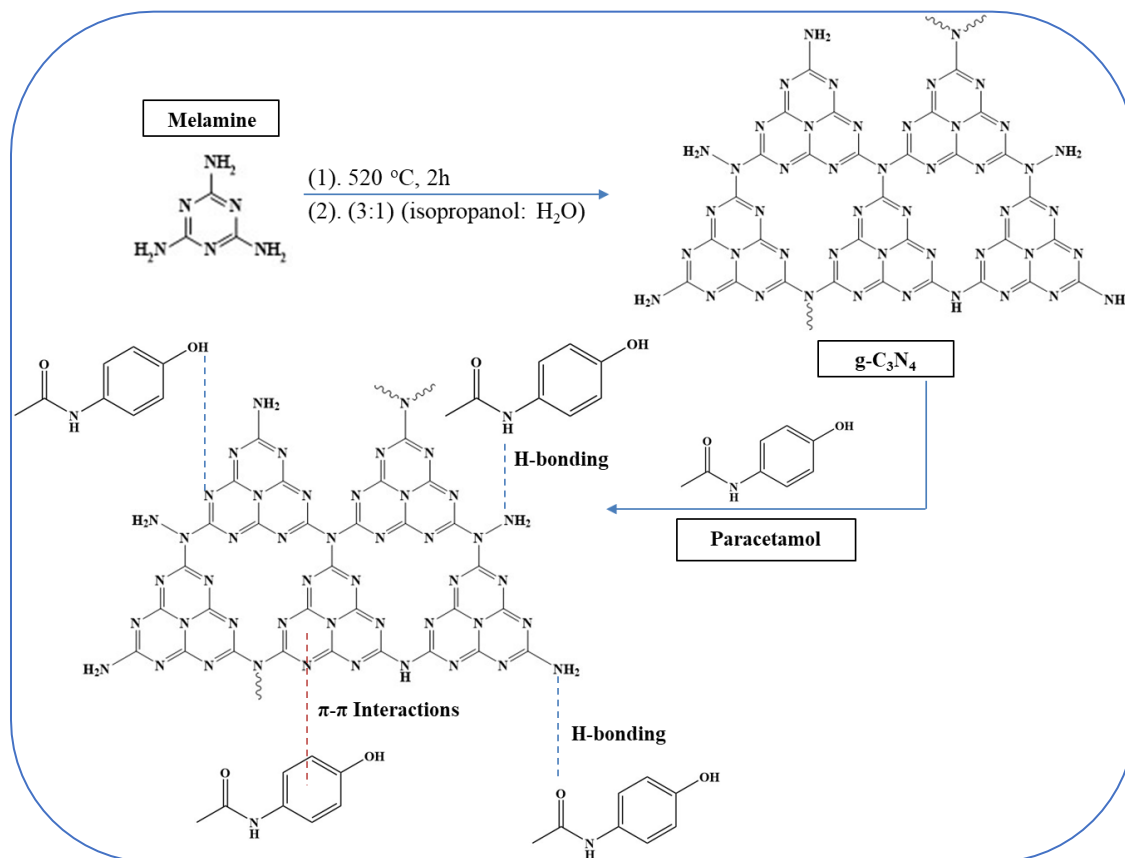
$$q_t = \frac{(C_0 - C_t)}{C_0} \times \frac{V}{W} \quad (3)$$

Where C_0 is the Initial drug concentration (mg/L), C_e is the Equilibrium drug concentration (mg/L), V is Solution volume (L), q_t is the adsorbed amount (mg/g), C_t is the concentration at time t (mg/L), and W is Adsorbent weight (g).

2.5. Instrumentation: To elucidate the structural and morphological properties of the synthesized g-C₃N₄ nanosheets, a suite of characterization techniques was employed. Crystal Structure: XRD using a Shimadzu XRD-LabX-600 diffractometer with Cu K α radiation ($\lambda = 1.54056 \text{ \AA}$) was utilized to assess the crystalline structure. The operating conditions were set at 40 mA/30 kV, with a scanning range of $2\theta = 5-80^\circ$ and a scan speed of 2° per minute. Morphology: TEM using a JEOL JEM-2100F HRTEM operated at 120 kV provided further insights into the nanosheets' morphology. A 1 μL aliquot of the suspension in methanol was placed on a Cu grid and dried under vacuum at 80°C overnight before TEM analysis. Functional Groups: FTIR using a Shimadzu Prestige 21 instrument was employed to identify and characterize functional groups present on the nanoparticles in the range of $450-4000 \text{ cm}^{-1}$. Optical Properties: UV-Vis absorbance spectra were recorded using an Agilent HP-8453 optics system equipped with a Hydrogen-Deuterium lamp for ultraviolet light and a Tungsten lamp for visible light.

2.6. Computational Study: DFT calculations, performed using the DMol3 module of the Materials Studio software (V2022) with the generalized gradient approximation (GGA) function at Perdew–Burke–Ernzerh (PBE) level for optimization, and MD simulation (Adsorption locator) module was employed to investigate the adsorption of drugs onto graphitic carbon nitride (g-C₃N₄). [15, 16] This research aimed to understand the underlying interaction mechanisms and optimize g-C₃N₄ for environmental applications.

3. Results and Discussions



Scheme 1. Procedure to prepare g-C₃N₄ from melamine by thermal decomposition at 520 °C and the possible pathways for paracetamol adsorption.

3.1. Material Design and Characterizations: g-C₃N₄ can be synthesized from melamine through a thermal decomposition process at 520°C as summarized in **Scheme 1**. This reaction involves the condensation and polymerization of melamine molecules, forming a highly conjugated polymer structure. The resulting g-C₃N₄ material exhibits a layered structure similar to graphite, with its unique electronic properties and large surface area making it an excellent candidate for various applications, including adsorption.[12, 17] The ability of g-C₃N₄ to absorb paracetamol is due to its polar surface and the presence of nitrogen-containing functional groups, which can interact with the polar functional groups of paracetamol. This interaction, mainly through hydrogen bonding and dipole-dipole forces, enables the effective adsorption of acetaminophen molecules onto the surface of g-C₃N₄. In addition, π - π interactions between the electron-rich π systems of aromatic rings can contribute to the adsorption process. These interactions can occur in either a parallel or perpendicular arrangement. Hydrogen bonding is a strong dipole-dipole interaction between a hydrogen atom bonded to a highly electronegative atom (e.g., oxygen, nitrogen) and another electronegative atom.[8, 18]

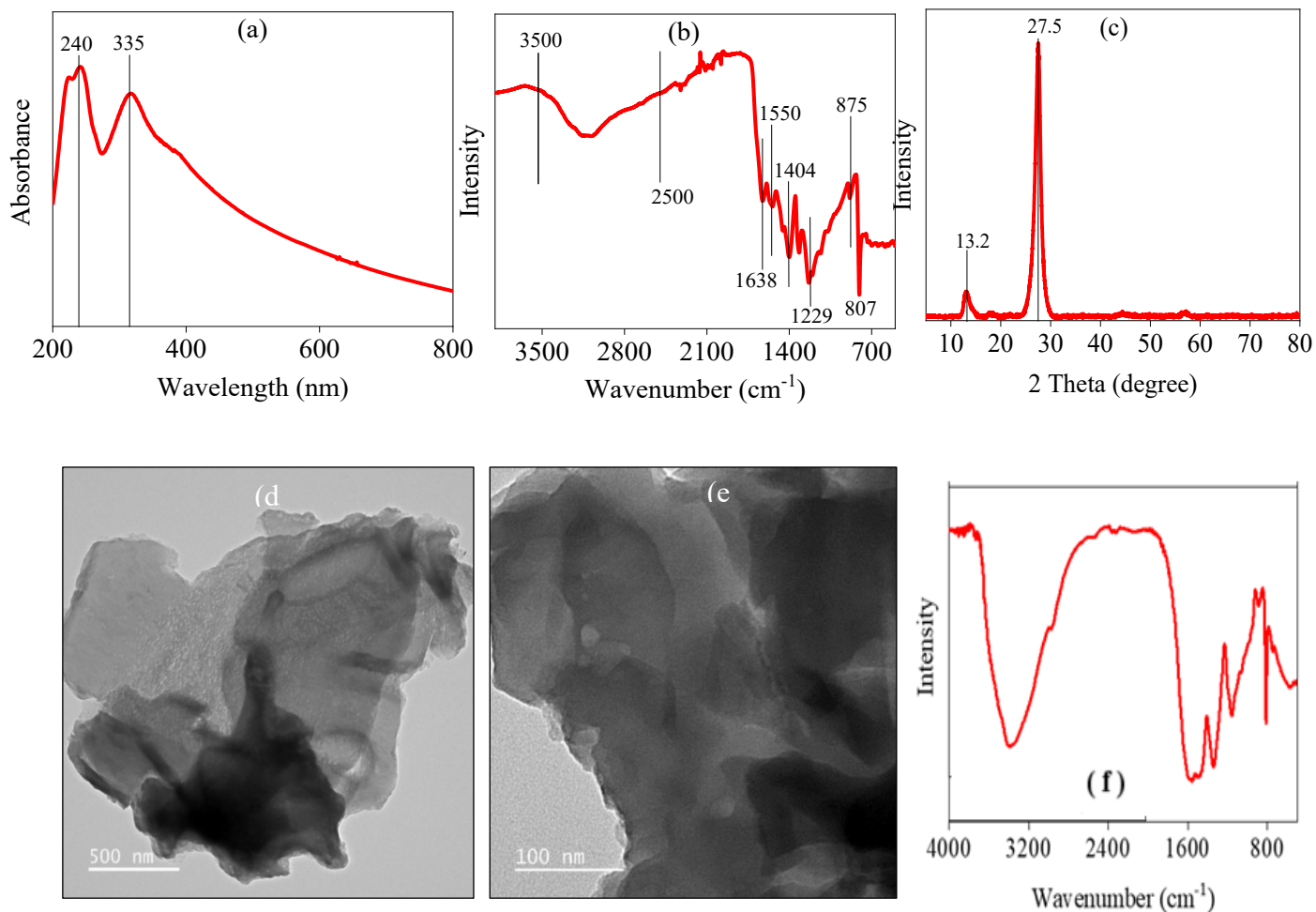


Figure 1. Characterization of $g\text{-C}_3\text{N}_4$: (a) UV-Vis spectrum, (b) FTIR spectrum of $g\text{-C}_3\text{N}_4$, (c) XRD patterns, (d, e) TEM images and (f) FTIR spectrum of $g\text{-C}_3\text{N}_4$ after adsorption of paracetamol.

3.2. Adsorbent Characterization: The synthesized $g\text{-C}_3\text{N}_4$ was characterized using various analytical techniques, including UV-VIS, FTIR, XRD, and TEM. UV-Vis spectroscopy was employed to determine its electronic properties. As shown in **Figure 1a**, the UV-Vis spectrum of $g\text{-C}_3\text{N}_4$ exhibits absorption peaks characteristic of a semiconductor, with wavelengths ranging from 200 to 450 nm. These peaks are attributed to the transfer of electrons from the nitrogen 2p orbitals in the valence band to the carbon 2p orbitals in the conduction band. Additionally, a sharp peak at 240 nm is associated with (n to π^*) transitions, while another peak at 335 nm is due to (n to π^*) transitions arising from electron transfer from nitrogen nonbonding orbitals to aromatic anti-bonding orbitals.[13, 19] FTIR spectroscopy was used to characterize the surface functional groups of $g\text{-C}_3\text{N}_4$. As depicted in **Figure 1b**, the FTIR spectrum of $g\text{-C}_3\text{N}_4$ showed two prominent peaks at 813 and 886 cm^{-1} indicative of triazine ring vibrations. C-N stretching vibrations were confirmed by peaks around 1630-1640 cm^{-1} and 1500-1550 cm^{-1} . C-H stretching vibrations, if present, may be observed around 3200-3400 cm^{-1} . Similarly, N-H stretching vibrations can be detected around 3300-3500 cm^{-1} if amino or imino groups are present. XRD analysis

was conducted to investigate the crystallinity of g-C₃N₄. [20, 21] As shown in **Figure 1c**, the XRD pattern revealed sharp peaks, indicating a crystalline structure. A prominent peak at $2\theta = 28.0^\circ$ corresponds to the stacking of (022) planes, while a weaker peak at $2\theta = 13.3^\circ$ is attributed to the (100) planes of heptazine repeating units in g-C₃N₄. The morphology of g-C₃N₄ was examined using TEM. As depicted in **Figures 1d** and **1e**, the TEM images revealed a sheet-like structure for the g-C₃N₄ nanosheets. These thin, flat sheets often stack on top of each other, forming a layered structure reminiscent of graphite. [12, 18]. After paracetamol adsorption (**Figure 1f**), the FTIR spectrum reveals notable changes, confirming interactions between paracetamol and g-C₃N₄. A new band near 1660 cm^{-1} appears, corresponding to the C=O stretch of the amide group in paracetamol. The broad band between $3000\text{--}3500\text{ cm}^{-1}$, associated with O–H and N–H stretching, shows increased intensity and a slight shift, suggesting hydrogen bonding between paracetamol's phenolic group and nitrogen sites on g-C₃N₄. Additional bands emerge at 1590 cm^{-1} and 1500 cm^{-1} , likely due to aromatic ring vibrations from paracetamol, while the band at 1230 cm^{-1} may arise from C–O stretching in the phenolic group. These modifications—new peaks, shifted intensities, and altered band positions—collectively demonstrate successful paracetamol adsorption. The interactions likely involve hydrogen bonding (e.g., O–H···N or N–H–N) and π – π stacking between paracetamol's aromatic ring and g-C₃N₄'s conjugated structure.

3.3. Adsorption Results

3.3.1. The Effect of Initial pH: The point of zero charge (PZC) of g-C₃N₄ at 4.3 (**Figure 2a**) indicates that its surface is positively charged at pH values below 4.3 and negatively charged above it. Paracetamol, being a weak acid with a pK_a around 9.5, primarily exists in its neutral form at pH values below its pK_a. As the pH increases towards the PZC, the positive surface charge of g-C₃N₄ decreases, reducing electrostatic repulsion and promoting adsorption. This is evident in **Figure 2b**, where the adsorption efficiency (R_e) increases significantly as the pH approaches the PZC. However, at pH values significantly above the PZC, the negatively charged g-C₃N₄ surface may repel the anionic form of paracetamol, which starts to form as the pH approaches the pK_a of paracetamol. This leads to a decrease in adsorption efficiency, as observed in **Figure 2b** at higher pH values. Therefore, the optimal pH for paracetamol adsorption onto g-C₃N₄ lies around the PZC, where the balance between electrostatic interactions and other adsorption mechanisms is favorable. This optimal pH range is approximately 4-6, as indicated by the peak in the adsorption efficiency curve in **Figure 2b**. [22, 23]

3.3.2. The Effect of Concentration and Adsorption Isotherms: To investigate the adsorption capacity of g-C₃N₄ for paracetamol, experiments were carried out at varying initial concentrations. As depicted in **Figure 2c**, the amount of paracetamol adsorbed increased with increasing initial concentration, reaching a maximum of 1.11 mg/g. This trend can be explained by the Langmuir adsorption isotherm, which is expressed by **Equation 4**. [24]

$$\frac{1}{q_e} = \frac{1}{bq_m} + \frac{1}{q_m} C_e \quad (4)$$

$$R_L = \frac{1}{1 + bC_0} \quad (5)$$

Where: C_e is the equilibrium concentration of the solute (mg/L), q_e is the amount of solute adsorbed per unit mass of adsorbent (mg/g), b is Langmuir constant related to the affinity between the adsorbent and adsorbate (L/mg), q_m is the maximum adsorption capacity (mg/g). The dimensionless equilibrium parameter (R_L) is a crucial characteristic of the Langmuir isotherm, given by **Equation 5**. [25]

Table 1. Parameters of the Langmuir-isotherms model for the Adsorption of paracetamol on g-C₃N₄.

R^2	b (L/mg)	$q_{\max, \text{fitted}}$	q_{exp}	R_L
0.9998	76.69	1.10	1.11	0.012

The experimental data exhibited excellent agreement with the Langmuir model, as shown in **Figure 2d** and **Table 1**. The high correlation coefficient ($R^2 = 0.9998$) and favorable R_L values ($0 < R_L < 0.1$) further support the Langmuir model's applicability. The calculated maximum adsorption capacity (q_{\max}) from the Langmuir model (1.10 mg/g) is in close agreement with the experimental data (1.1 mg/g), reinforcing the monolayer adsorption mechanism. The exceptional adsorption performance of g-C₃N₄ for paracetamol can be attributed to its high surface area and the presence of nitrogen-containing functional groups, such as amino groups. These functional groups facilitate strong hydrogen bonding and electrostatic interactions with paracetamol, leading to efficient adsorption.

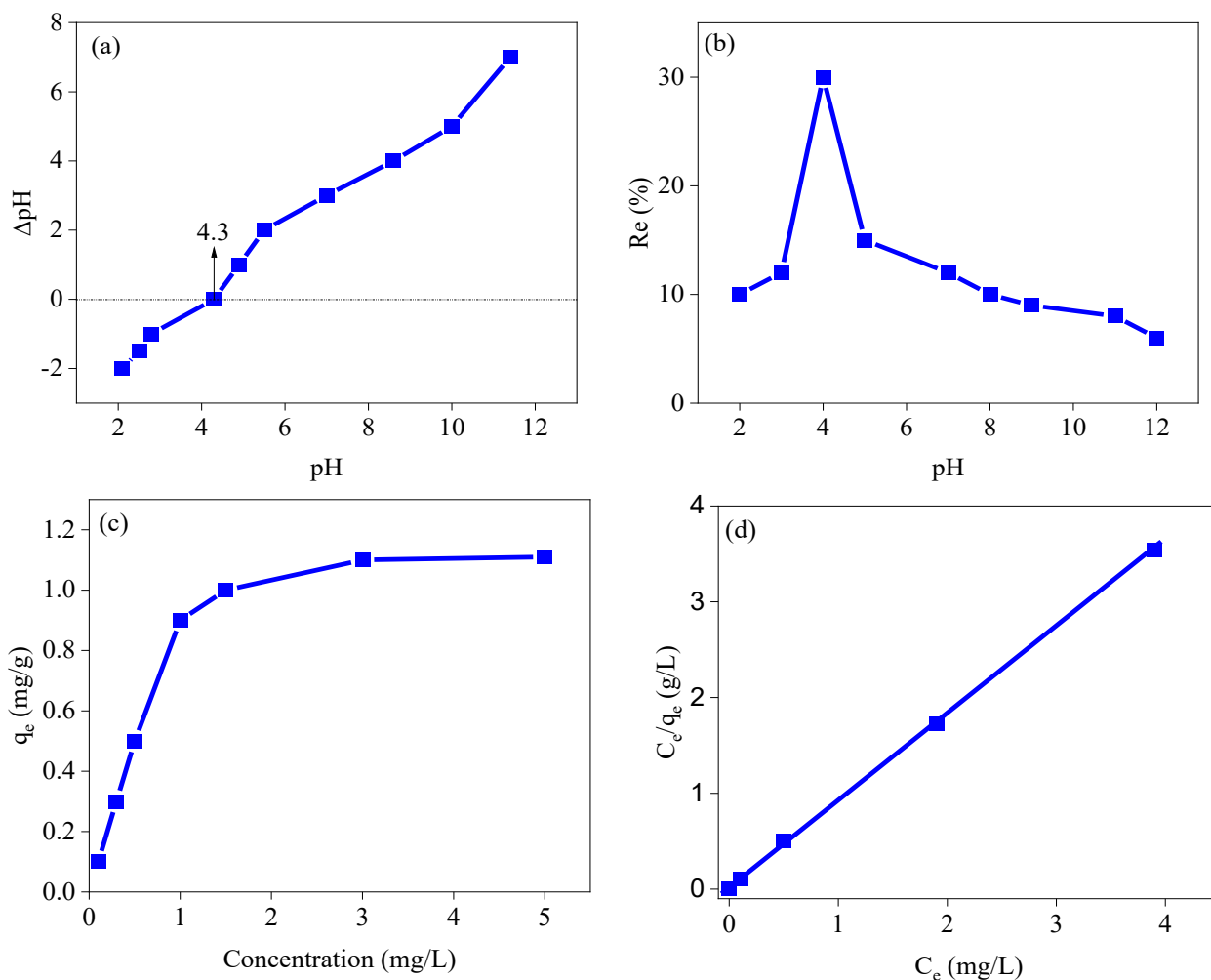


Figure 2. The effect of pH on the adsorption of paracetamol onto g-C₃N₄. (a) shows the point of zero charge (PZC) of g-C₃N₄, which is 4.3. (b) shows the adsorption efficiency of paracetamol onto g-C₃N₄ as a function of pH. (c) the effect of concentration on the adsorption of paracetamol onto g-C₃N₄ [Conditions: $C_0 = 0.1, 0.3, 0.5, 1, 1.5, 3, 5$ ppm, pH = 4, $T = 298$ K, $t = 420$ min, adsorbent dose = 0.01 g/10 mL]. (d) Langmuir isotherm model for the adsorption.

3.3.3. The Effect of Contact Time and Adsorption Kinetics: Adsorption is a time-dependent process, and the impact of contact time can significantly influence the overall efficiency. This study investigated the effect of contact time within 30 to 180 minutes. As illustrated in **Figure 3a**, the adsorption rate was initially slow, but accelerated notably after 15 minutes, reaching equilibrium at approximately 60 minutes. Beyond this point, no further adsorption was observed, and even desorption might have occurred. This behavior can be attributed to the gradual saturation of active sites on the adsorbent surface. As the surface becomes increasingly occupied, the availability of free sites decreases, leading to a decline in the adsorption rate.[9, 26] Kinetic modeling was employed to gain insights into the underlying mechanisms of the adsorption process. The pseudo-second-order kinetic model was used as in **Equation 6**. Where: k_2

($\text{g}\cdot\text{mole}^{-1}\cdot\text{min}^{-1}$) is the second-order rate constant of adsorption, q_e and q_t are the adsorbed amount (mg/g) at equilibrium and at time t (min), respectively.[24]

$$\frac{t}{q_t} = \frac{1}{k_2 q_e^2} + \frac{t}{q_e} \quad (6)$$

The results in **Figure 3b** and **Table 2** best fit the experimental data, as evidenced by the high correlation coefficient ($R^2 = 0.9866$) and the close agreement between the calculated and experimental equilibrium adsorption capacities ($q_{e, \text{fitted}}$ and $q_{e, \text{exp}}$). This suggests that the rate-limiting step in the adsorption process involves the interaction between the adsorbate molecules and the active sites on the adsorbent surface.

Table 2. Kinetic Parameters for Adsorption of Paracetamol on $g\text{-C}_3\text{N}_4$.

R^2	$q_{\text{max, fitted}}$	q_{exp}	k_2
0.9866	0.568	0.500	0.10173

3.3.4. The Effect of Temperature and Adsorption Thermodynamics: The impact of temperature on the adsorption capacity of paracetamol onto $g\text{-C}_3\text{N}_4$ was investigated. Experiments were conducted at pH 4, with a contact time of 420 minutes, a $g\text{-C}_3\text{N}_4$ dosage of 10 mg/L, and paracetamol concentrations ranging from 0.1 to 5 mg/L. Three temperatures were tested: 25, 35, and 50 °C. As the temperature increased, the maximum adsorption capacity rose from 1.1 to 3.2 mg/g as **Figure 3c** shows, likely due to increased molecular mobility and kinetic energy at higher temperatures.[26] Thermodynamic parameters (ΔH , ΔS , and ΔG) were determined using **Equations 7 and 8**. Where ΔG° represents the change in free energy, ΔH° represents the change in enthalpy, ΔS° represents the change in entropy, R is the gas constant, T is the temperature, and K_c is the equilibrium constant.[27, 28]

$$\Delta G^\circ = -RT \ln K_c \quad (7)$$

$$\ln K_c = \left(\frac{\Delta S^\circ}{R}\right) - \left(\frac{\Delta H^\circ}{R}\right) \frac{1}{T} \quad (8)$$

The data and the calculated thermodynamic parameters are presented in **Figure 3d** and **Table 3**, respectively. The negative ΔG values indicate that the adsorption process is spontaneous and favorable at all temperatures, with the process becoming more favorable at higher temperatures. This suggests a potential expansion of adsorbent pores at higher temperatures, facilitating increased diffusion of paracetamol molecules. The positive ΔH value confirms the endothermic nature of the process, consistent with the increased adsorption capacity at higher temperatures. Additionally, the positive ΔS value suggests an increase in disorder at the solid-solution interface during adsorption.[23, 26] These findings indicate a strong affinity between paracetamol and the $g\text{-C}_3\text{N}_4$ adsorbent, with the adsorption mechanism primarily physical in nature.

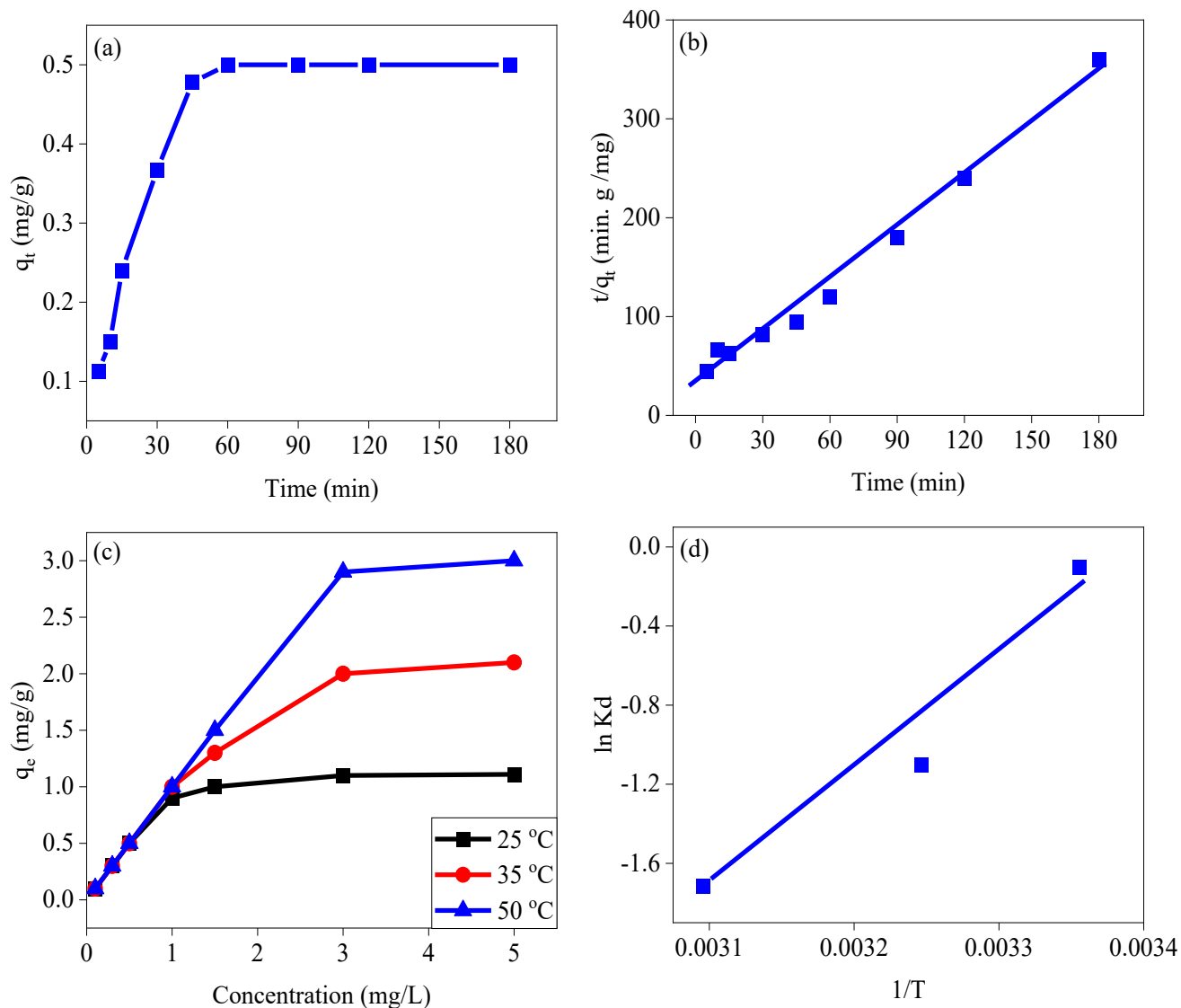


Figure 3: (a) Impact of contact time on paracetamol removal by g-C₃N₄ (pH 4, adsorbent dose = 0.001 g/10 mL, T = 298 K). (b) Pseudo-second-order kinetic model for paracetamol adsorption onto g-C₃N₄. (c) Influence of temperature on paracetamol removal by g-C₃N₄ (pH 4, adsorbent dose = 0.001 g/10 mL, T = 298, 308, 323 K, t = 420 min). (d) Thermodynamic assessment via Van't Hoff plot reveals the endothermic nature of paracetamol adsorption on g-C₃N₄ ($\Delta H^\circ > 0$).

Table 3: Thermodynamic parameters for the adsorption of paracetamol on g-C₃N₄.

ΔG (kJ mol ⁻¹)			ΔH (kJ mol ⁻¹)	ΔS (kJ mol ⁻¹ T ⁻¹)	R^2
298 K	308 K	323 K	48.356	0.1509	0.9987
-21.059	-23.456	-27.525			

3.5. Theoretical calculation Results: DFT was employed to investigate the adsorption of drugs onto g-C₃N₄, [29-32] aiming to elucidate the underlying interaction mechanisms and optimize this material for environmental remediation applications. The favorable interaction between g-C₃N₄ and paracetamol is likely attributed to the unique surface chemistry and structural features of g-C₃N₄, which enhance its affinity for organic molecules. [33] Structural interactions between paracetamol and g-C₃N₄ are likely mediated through π - π stacking and hydrogen bonding, with the triazine groups of g-C₃N₄ playing a crucial role in governing the adsorption efficiency. DFT provides valuable insights into the stability and electronic properties of the g-C₃N₄-drug complex. The calculations reveal that adsorption induces alterations in electron density and facilitates charge transfer, which is critical for understanding the adsorption process and optimizing g-C₃N₄ for efficient drug removal from water. [32, 34].

Table 4: DFT calculated parameters from Optimization processes for Paracetamol, g-C₃N₄, and Paracetamol-g-C₃N₄ complex.

Parameter		g-C ₃ N ₄	Paracetamol	g-C ₃ N ₄ -Paracetamol complex
(E _{LUMO})	E _{HOMO}	-5.706	-4.921	-5.031
(E _{HOMO})	E _{LUMO}	-3.436	-1.12	-3.481
(ΔE_g)	$\Delta E_{(HOMO-LUMO)}$	-2.27	-3.801	-1.55
(I)	Ionization energy (I)	5.706	4.921	5.031
(A)	Electron affinity (A)	3.436	1.12	3.481
(η)	Electronegativity (X)	4.571	3.021	4.256
(χ)	Global hardness (η)	1.135	1.901	0.775
(μ)	Chemical potential (μ)	-4.571	-3.021	-4.256
(σ)	Global softness (σ)	0.881	0.526	1.290
(ω)	Global electrophilicity (ω)	9.204	2.400	11.686
($\omega +$)	Electroaccepting ($\omega+$) power	7.061	1.128	9.655
($\omega -$)	Electrodonating ($\omega-$) power	11.632	4.148	13.911
($\omega \pm$)	Net electrophilicity ($\Delta\omega+-$)	18.692	5.276	23.566
(ϵ)	Nucleophilicity (ϵ)	0.109	0.417	0.086
(Q _{max})	Fraction of transferred electrons (ΔN)	-2.014	-0.795	-2.746
(ΔN)	Electronic charge accepting capability Q _{max}	4.027	1.589	5.492
E _f	Formation energy (eV)	-490.217	-101.818	-591.031

Table 4 summarizes the electronic parameters derived from the optimization of paracetamol, g-C₃N₄, and their complex. The data reveals that the interaction between g-C₃N₄ and paracetamol results in shifts in both the highest occupied molecular orbital (HOMO) and lowest unoccupied molecular orbital (LUMO) energies, signifying a modification of the electronic structure upon complexation. The observed decrease in the energy gap (ΔE_g) between HOMO and LUMO for the complex suggests the formation of a more stable compound with lower energy. The ionization energy of the complex lies between those of paracetamol and g-C₃N₄, indicating a balanced electronic interaction. Conversely, the electron affinity of the complex is closer to that of g-C₃N₄, suggesting that g-C₃N₄ primarily governs the electron-accepting behavior of the complex. The reduced global hardness of the complex implies increased reactivity and a higher likelihood of interaction. Its electronegativity falls within an intermediate range, signifying a balanced distribution of electron density. The complex's chemical potential aligns more closely with that of g-C₃N₄, indicating that g-C₃N₄ exerts a significant influence on the overall chemical behavior of the complex. Furthermore, the increased global softness of the complex suggests enhanced reactivity and flexibility. The elevated net electrophilicity of the complex points towards a higher overall reactivity. Conversely, the observed decrease in nucleophilicity implies a reduced tendency to donate electrons in the complex.

Table 5 . Lower adsorption configuration output results from the Adsorption Locator model.

Structures	Total energy <i>kcal mol⁻¹</i>	Adsorption energy <i>kcal mol⁻¹</i>	Rigid adsorption energy <i>kcal mol⁻¹</i>	Deformation energy <i>kcal mol⁻¹</i>	dE_{ad}/dN_i <i>kcal mol⁻¹</i>
Paracetamol + g-C ₃ N ₄	-85.696×10^3	-38.640×10^3	-36.000×10^3	-2.643	-38.640

The adsorption study reveals an electrostatic attraction between paracetamol and the g-C₃N₄ surface, evidenced by an increase in the bond lengths of NH and CN groups within g-C₃N₄ due to the interaction with paracetamol. The formation of hydrogen bonds (Paracetamol) N-H...N-H (g-C₃N₄) is likely, supported by the short distances observed between the nearest H and N atoms (1.678, 3.079, and 2.786 Å) after adsorption, as depicted in **Figure 4**, which confirms the FTIR results shown in **Figure 1f**. MD simulations indicate a strong interaction between paracetamol and g-C₃N₄, corroborated by the parameter analysis. The negative values for total energy, adsorption energy, and rigid adsorption energy in **Table 5** suggest a stable complex with strong intermolecular interactions. Furthermore, the low deformation energy confirms the stability of the complex by indicating minimal structural changes in the molecules during adsorption. These computational results are consistent with the experimental findings.

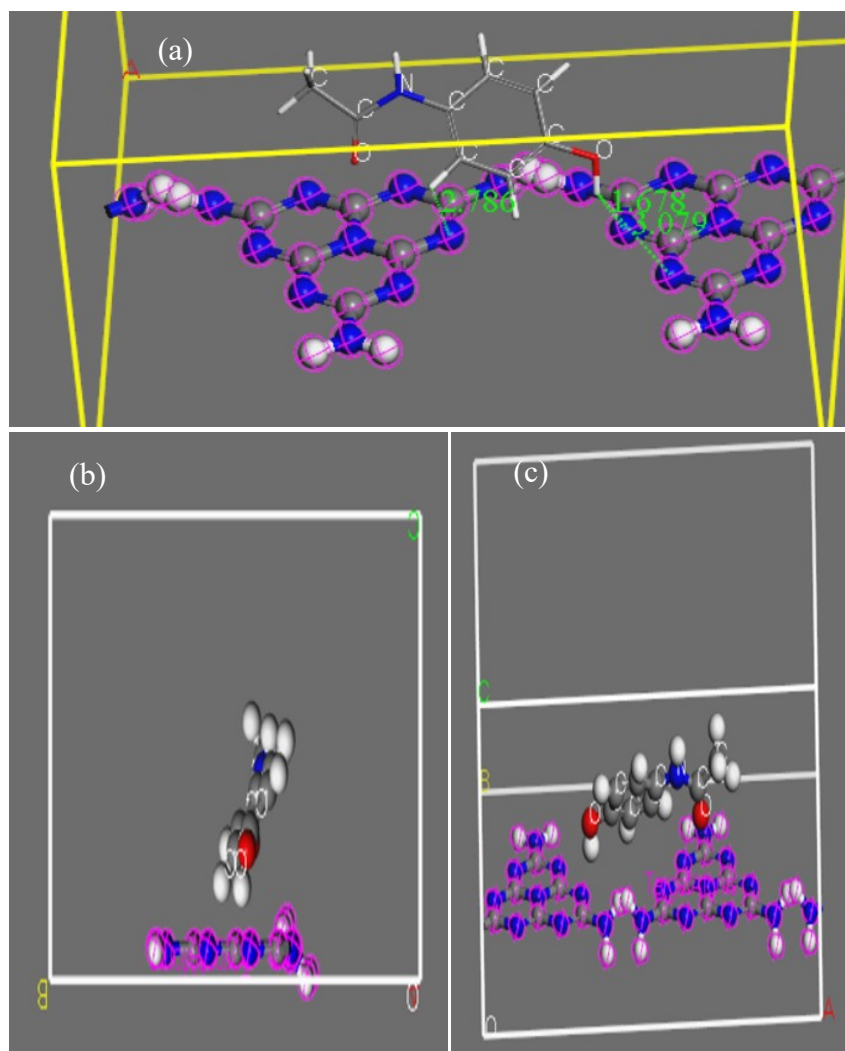


Figure 4. (a) The obtained energies for the most stable complex, (a) top view and (b) side view of the adsorption adsorbed paracetamol-g-C₃N₄ complex.

4. Conclusions and Outlooks

This study successfully demonstrated the feasibility of employing cost-effective raw graphitic carbon nitride for paracetamol removal from water. Comprehensive material characterization via XRD, XRF, FT-IR, and TEM elucidated the adsorbent's properties. Systematic investigation of key operational parameters, including pH, contact time, adsorbent dosage, and initial paracetamol concentration, revealed a maximum adsorption capacity of 1.1 mg/g achieved at 25°C within 60 minutes. The adsorption process was well-described by both Langmuir and pseudo-second-order kinetic models. Complementary DFT calculations confirmed the stability of the paracetamol-g-C₃N₄ complex, while MD simulations indicated a high propensity for hydrogen bond formation, yielding a calculated adsorption energy of -38.640×10^{-3} kcal/mol. The strong synergy between these experimental and computational findings highlights the

significant potential of raw graphitic carbon nitride as an environmentally benign and economical adsorbent for pharmaceutical contaminant removal from aqueous solutions. Future research should explore its efficacy in treating real wastewater samples and investigate the regeneration capabilities of the spent adsorbent to further establish its practical applicability.

References

- [1] Hejna, M., D. Kapuścińska, and A. Aksmann, *Pharmaceuticals in the Aquatic Environment: A Review on Eco-Toxicology and the Remediation Potential of Algae*. Int J Environ Res Public Health, 2022. **19**(13).
- [2] Eapen, J.V., et al., *A review of the effects of pharmaceutical pollutants on humans and aquatic ecosystem*. Exploration of Drug Science, 2024. **2**(5): p. 484-507.
- [3] Quesada, H.B., et al., *Surface water pollution by pharmaceuticals and an alternative of removal by low-cost adsorbents: A review*. Chemosphere, 2019. **222**: p. 766-780.
- [4] Pacheco-Álvarez, M., et al., *A critical review on paracetamol removal from different aqueous matrices by Fenton and Fenton-based processes, and their combined methods*. Chemosphere, 2022. **303**: p. 134883.
- [5] Al-howri, B.M., et al., *Paracetamol in diverse water sources: health hazards and treatment efficacy emphasizing adsorption techniques—a review*. International Journal of Environmental Science and Technology, 2024. **21**(15): p. 9743-9762.
- [6] Ivanova, D., G. Tzvetkov, and N. Kaneva *Degradation of Paracetamol in Distilled and Drinking Water via Ag/ZnO Photocatalysis under UV and Natural Sunlight*. Water, 2023. **15**, DOI: 10.3390/w15203549.
- [7] Islam, M., et al., *Adsorptive removal of paracetamol from aqueous media: A comprehensive review of adsorbent materials, adsorption mechanisms, recent advancements, and future perspectives*. Journal of Molecular Liquids, 2024.
- [8] Aminul Islam, M., et al., *Adsorptive removal of paracetamol from aqueous media: A review of adsorbent materials, adsorption mechanisms, advancements, and future perspectives*. Journal of Molecular Liquids, 2024. **396**: p. 123976.
- [9] Spaltro, A., et al., *Removal of paracetamol from aqueous solution by activated carbon and silica. Experimental and computational study*. Journal of Contaminant Hydrology, 2021. **236**: p. 103739.
- [10] Maneewong, Y., et al., *Paracetamol removal from water using N-doped activated carbon derived from coconut shell: Kinetics, equilibrium, cost analysis, heat contributions, and molecular-level insight*. Chemical Engineering Research and Design, 2022. **185**: p. 163-175.
- [11] Yılmaz, Ş., A. Zengin, and T. Şahan, *Effective utilization of Fe(III)-based metal organic framework-coated cellulose paper for highly efficient elimination from the liquid phase of paracetamol as a pharmaceutical pollutant*. Environmental Technology & Innovation, 2021. **24**: p. 101799.
- [12] Zhao, Z., Y. Sun, and F. Dong, *Graphitic carbon nitride based nanocomposites: a review*. Nanoscale, 2015. **7**(1): p. 15-37.
- [13] Zhao, G.-Q., et al., *A critical review on graphitic carbon nitride (g-C₃N₄)-based composites for environmental remediation*. Separation and Purification Technology, 2021. **279**: p. 119769.
- [14] Alaghmandfard, A. and K. Ghandi, *A Comprehensive Review of Graphitic Carbon Nitride (g-C₃N₄)-Metal Oxide-Based Nanocomposites: Potential for Photocatalysis and Sensing*. Nanomaterials, 2022. **12**(2): p. 294.
- [15] Bicheng, Z., et al., *Adsorption investigation of CO₂ on g-C₃N₄ surface by DFT calculation*. Journal of CO₂ Utilization, 2017. **21**: p. 327-335.
- [16] Iqbal, J., et al., *DFT study of therapeutic potential of graphitic carbon nitride (g-C₃N₄) as a new drug delivery system for carboplatin to treat cancer*. Journal of Molecular Liquids, 2021. **331**: p. 115607.

- [17] Zhu, J., et al., *Graphitic Carbon Nitride: Synthesis, Properties, and Applications in Catalysis*. ACS Applied Materials & Interfaces, 2014. **6**(19): p. 16449-16465.
- [18] Fronczak, M., *Adsorption performance of graphitic carbon nitride-based materials: Current state of the art*. Journal of Environmental Chemical Engineering, 2020. **8**(5): p. 104411.
- [19] Ghalkhani, M., M.H. Khaneghah, and E. Sohoul, *Chapter 13 - Graphitic carbon nitride: Synthesis and characterization*, in *Handbook of Carbon-Based Nanomaterials*, S. Thomas, et al., Editors. 2021, Elsevier. p. 573-590.
- [20] Sunasee, S., et al., *Sonophotocatalytic degradation of bisphenol A and its intermediates with graphitic carbon nitride*. Environmental Science and Pollution Research, 2019. **26**: p. 1-12.
- [21] Ahmaruzzaman, M. and S.R. Mishra, *Photocatalytic performance of g-C₃N₄ based nanocomposites for effective degradation/removal of dyes from water and wastewater*. Materials Research Bulletin, 2021. **143**: p. 111417.
- [22] Bernal, V., et al., *Effect of Solution pH on the Adsorption of Paracetamol on Chemically Modified Activated Carbons*. Molecules, 2017. **22**: p. 1032.
- [23] Terzyk, A.P., *The influence of activated carbon surface chemical composition on the adsorption of acetaminophen (paracetamol) in vitro: Part II. TG, FTIR, and XPS analysis of carbons and the temperature dependence of adsorption kinetics at the neutral pH*. Colloids and Surfaces A: Physicochemical and Engineering Aspects, 2001. **177**(1): p. 23-45.
- [24] Azizian, S. and S. Eris, *Chapter 6 - Adsorption isotherms and kinetics*, in *Interface Science and Technology*, M. Ghaedi, Editor. 2021, Elsevier. p. 445-509.
- [25] Vedenyapina, M., et al., *Adsorption of Heavy Metals on Activated Carbons (A Review)*. Solid Fuel Chemistry, 2021. **55**: p. 83-104.
- [26] Awad, F.S., et al., *Thiol- and Amine-Incorporated UIO-66-NH₂ as an Efficient Adsorbent for the Removal of Mercury(II) and Phosphate Ions from Aqueous Solutions*. Industrial & Engineering Chemistry Research, 2021. **60**(34): p. 12675-12688.
- [27] Allaoui, I., et al., *Adsorption equilibrium, kinetic, and thermodynamic studies on the removal of paracetamol from wastewater using natural and HDTMA-modified clay*. Desalination and Water Treatment, 2024. **318**: p. 100345.
- [28] Haro, N.K., et al., *Kinetic, equilibrium and thermodynamic studies of the adsorption of paracetamol in activated carbon in batch model and fixed-bed column*. Applied Water Science, 2021. **11**(2): p. 38.
- [29] Perveen, M., et al., *Therapeutic potential of graphitic carbon nitride as a drug delivery system for cisplatin (anticancer drug): A DFT approach*. Biophysical Chemistry, 2020. **267**: p. 106461.
- [30] Shamim, M., et al., *DFT study of therapeutic potential of graphitic carbon nitride (g-C₃N₄) as a new drug delivery system for carboplatin to treat cancer*. Journal of Molecular Liquids, 2021. **331**: p. 115607.
- [31] Perveen, M., et al., *DFT study of therapeutic potential of graphitic carbon nitride as a carrier for controlled release of melphalan: an anticancer drug*. Journal of Molecular Modeling, 2022. **28**(11): p. 359.
- [32] Negro, P., et al., *Combined DFT-D3 computational and experimental studies on g-C₃N₄: New insight into structure, optical, and vibrational properties*. Materials, 2023. **16**(10): p. 3644.
- [33] Jiménez-Salcedo, M., M. Monge, and M.T. Tena, *An organometallic approach for the preparation of Au-TiO₂ and Au-g-C₃N₄ nanohybrids: improving the depletion of paracetamol under visible light*. Photochemical & Photobiological Sciences, 2022. **21**(3): p. 337-347.
- [34] Luo, S., et al., *Effect of Pt doping on sensing performance of g-C₃N₄ for detecting hydrogen gas: a DFT study*. Vacuum, 2022. **200**: p. 111014.



Analysis of Magnetic Properties and Critical Current Density of Tl-2234 High-Temperature Superconductor Using AC Magnetic Susceptibility Measurements

Belqees Hassan*

Department of Physics, College of Science, Qassim University, Buraydah 51452, Saudi Arabia

*Corresponding author: (B. Hassan), *Email Address:* B.hassan@qu.edu.sa

Abstract

This study investigates the magnetic properties and critical current density of $\text{Tl}_2\text{Ba}_2\text{Ca}_3\text{Cu}_4\text{O}_{11+\delta}$ (Tl-2234) high-temperature superconductors through AC magnetic susceptibility measurements. Samples were synthesized using a one-step solid-state process with careful thermal treatment protocols to minimize thallium evaporation. AC susceptibility measurements were conducted across temperatures ranging from 140-50K under various applied AC magnetic fields (0.5-8 mT). The analysis revealed distinct transitions in both real (χ') and imaginary (χ'') components of susceptibility, providing insights into intragranular superconductivity and intergranular coupling. The imaginary component peaks shifted towards lower temperatures with increasing magnetic field strength, indicating enhanced magnetic strength within grains and increased intra-grain pinning centers. Using Bean's critical-state model, the critical current density (J_c) was calculated from the peak positions in $\chi''(T)$ curves. The temperature dependence of J_c followed an empirical scaling relation, yielding a zero-temperature critical current density $J_c(0)$ of 3.6×10^5 A/cm² and a critical exponent of 1.26 ± 0.078 . These findings contribute to understanding the correlations between structural characterization and magnetic properties in Tl-2234 superconductors, which is crucial for their potential applications in high-field and high-temperature environments.

Keywords: AC magnetic susceptibility; Current density; Flux pinning; Magnetic properties; structural characterization.

<https://doi.org/10.63070/jesc.2025.003>

Received 28 March 2025; Revised 28 April 2025; Accepted 13 May 2025.

Available online 21 May 2025.

Published by Islamic University of Madinah on behalf of *Islamic University Journal of Applied Sciences*. This is a free open access article.

1. Introduction

High-temperature superconductors (HTS) have emerged as materials of substantial scientific significance, owing to their transformative potential in energy-efficient technological applications, encompassing power transmission infrastructure, magnetic resonance imaging (MRI) systems, and magnetic levitation technologies [1,2]. Within the broader classification of HTS materials, copper oxide-based (cuprate) superconductors demonstrate remarkable characteristics at operational temperatures substantially exceeding the liquid nitrogen boiling threshold (77 K), conferring distinct practical advantages over conventional superconducting systems [3]. Specifically, thallium-based cuprates (TBCCO) stand out for their relatively high critical temperature (T_c), which can be achieved under ambient pressure [4]. Within this family, the compound (Tl-2234) has gained attention due to its unique structural features and promising superconducting properties. Structurally, Tl-2234 belongs to the Tl-1223 family and is characterized by alternating layers of TlO and CuO₂, which play a crucial role in its magnetic and electronic properties [5-8]. These layered structures, combined with various types of crystal defects such as oxygen vacancies and grain boundaries, significantly influence the material's flux pinning mechanisms and, consequently, its critical current density (J_c). The analysis of alternating-current magnetic susceptibility has established itself as a sophisticated analytical technique for elucidating the intricate magnetic phenomena exhibited by high-temperature superconducting materials. This technique provides essential information about flux pinning mechanisms, critical current densities, and intergranular coupling in these materials. The AC susceptibility response is characterized by both real (χ') and imaginary (χ'') components, offering complementary insights into magnetic shielding and energy dissipation processes, respectively. The temperature and field dependence of these components reveals crucial details about flux penetration, pinning strength, and energy dissipation. Additionally, higher harmonic components of the AC susceptibility are particularly sensitive to nonlinear effects arising from vortex motion and flux pinning, providing insights into vortex dynamics that are not accessible through DC measurements alone [9,10].

Despite the extensive research on Tl-2234, a comprehensive understanding of the correlations between its structural characteristics, AC magnetic susceptibility behavior, and critical current density remains incomplete. This knowledge gap is particularly significant given the material's potential for practical applications in high-field and high-temperature environments. This study aims to investigate the temperature and magnetic field dependence of AC susceptibility components (χ' and χ'') in Tl-2234, while

analyzing the correlation between structural defects and magnetic properties through higher harmonic susceptibility measurements.

2. Experimental Methods

2.1 Sample Preparation

The synthesis of $\text{Tl}_2\text{Ba}_2\text{Ca}_3\text{Cu}_4\text{O}_{11+\delta}$ was initiated through the careful selection of high-purity precursor materials, including thallium oxide (Tl_2O_3), barium peroxide (BaO_2), calcium oxide (CaO), and copper oxide (CuO). The preparation followed a standard one-step solid-state process, where stoichiometric quantities of these precursors were thoroughly mixed using an agate mortar. To ensure homogeneity, the resulting powder was passed through a 64 μm sieve. The homogeneous powder mixture was subsequently compressed into a disc-shaped pellet with dimensions of diameter 1.5 cm and thickness 0.2 cm.

2.2 Heat Treatment

To minimize thallium evaporation during the thermal treatment, the sample was carefully wrapped in silver foil. For safety considerations and to protect the furnace from potential hazardous effects, the wrapped sample was placed in a sealed quartz tube (diameter 1.5 cm \times length 15 cm), which was then enclosed within a protective stainless steel tube. The thermal processing methodology consisted of positioning the hermetically sealed specimen in a horizontal orientation within a furnace chamber, followed by controlled heating at a 6°C/min gradient until achieving 811°C. The specimen was held isothermally at this temperature for a duration of six hours, after which controlled cooling was implemented at 0.5°C/min until reaching ambient temperature. Superconducting characteristics were further optimized through supplementary thermal treatment in ambient atmosphere at 500°C.

2.3 Magnetic Measurements

Magnetic Characterization Magnetic measurements were conducted using a LakeShore Superconducting Magnet System integrated with a helium cryostat. AC magnetic susceptibility components (real and imaginary) were recorded across AC field amplitudes from 0.5 mT to 8 mT, spanning a temperature range of 50-140 K. Sample preparation involved mechanical grinding and size classification through an 89 μm mesh to ensure homogeneous particle distribution. It is important to clarify that the 89 μm mesh was used for particle size classification to ensure homogeneity of the sample, and this mesh size represents the

maximum size of particles that were allowed to pass through, effectively setting an upper limit on the particle size in the measured sample.

3. Results and Discussion

3.1 AC Magnetic Susceptibility Analysis

The complex AC magnetic susceptibility ($\chi = \chi' + i\chi''$) serves as a powerful analytical tool for investigating high-temperature superconductors, particularly in granular systems where both components (χ' and χ'') exhibit distinct temperature and field amplitude dependencies [11]. AC susceptibility measurements have gained popularity due to their simplicity, cost-effectiveness, and high sensitivity, enabling sophisticated quantitative analysis [12]. When exposed to a periodic field, $H_a(t) = h \sin(2\pi vt)$, the sample exhibits a magnetic moment in opposition to the applied field, expressed as [13]:

$$\chi(h, v) = \chi' + i\chi'' \quad (1)$$

Where v is the frequency. The real component (χ') approximates zero-field-cooling susceptibility in DC measurements, quantifying the superconductor's shielding response, while the imaginary component (χ'') reflects energy dissipation. In polycrystalline high- T_c materials, temperature-dependent AC susceptibility reveals two distinct transitions: the higher-temperature drop in χ' (intragranular superconductivity) and the

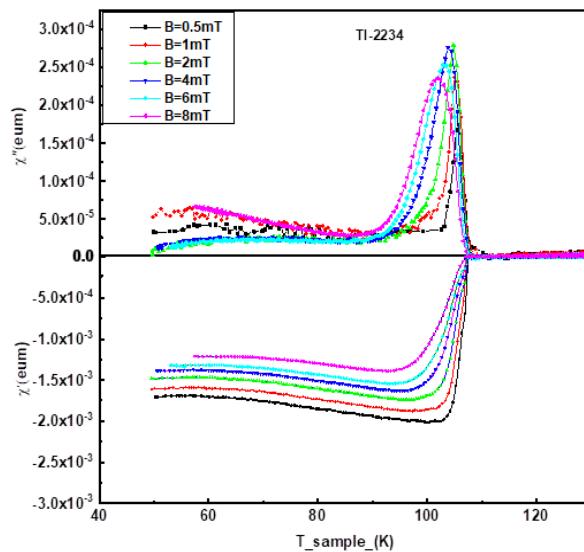


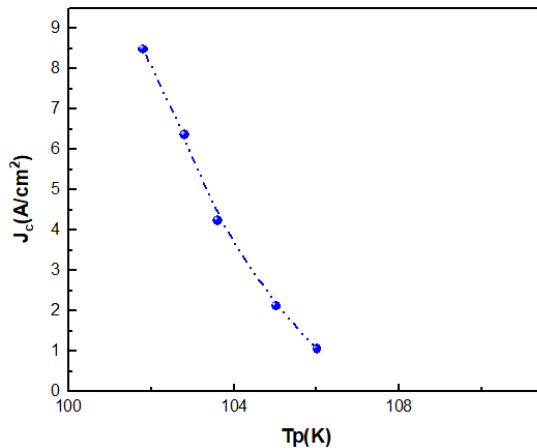
Figure 1. AC magnetic susceptibility vs. temperature for the powder sample TI-2234 under different AC field amplitudes.

lower-temperature drop (intergranular coupling) [14]. Figure 1 presents the temperature dependence of both real and imaginary components of AC magnetic susceptibility for the Tl-2234 sample under varying alternating magnetic fields.

The sample demonstrates a well-defined superconducting transition, characterized by a sharp response with minimal broadening in the transition region. The real component exhibits modest field-dependent broadening across the transition. Notable features in the data include systematic shifts of the χ'' peaks toward lower temperatures with increasing alternating magnetic field amplitude. This behavior can be attributed to two primary mechanisms: first, the enhanced magnetic field strength within the grains leads to increased activation of intra-grain pinning centers, resulting from a reduction in the effective superconducting volume fraction. Second, the progressive shift of the penetration temperature (T_p) to lower values with increasing field strength correlates with an expansion of the frozen volume fraction at inter-grain boundaries, consequently diminishing the overall superconducting phase fraction. These observations provide insights into both the intra-grain and inter-grain magnetic response of the Tl-2234 system. After presenting the AC susceptibility data, it is important to discuss the observed critical temperature (T_c) value of approximately 107 K, as shown in Figure 1. This value is somewhat lower than the commonly reported T_c range of 113-116 K for optimally doped and single-phase Tl-2234 compounds, as documented in the literature [15,16]. Several factors may explain this discrepancy. First, the oxygen stoichiometry in Tl-based cuprates is highly sensitive and can significantly impact superconducting properties, including T_c . Even minor deviations from the optimal oxygen content can lead to a reduction in T_c . Second, as noted in the introduction, Tl-based superconductors are susceptible to phase inhomogeneity and intergrowth of different Tl-Ba-Ca-Cu-O phases. The presence of minor secondary phases or intergrown members of the homologous series, even if not easily detectable by bulk techniques like AC susceptibility, can influence the overall superconducting behavior and potentially lower the observed T_c . Additionally, the method used to determine T_c can affect the measured value. In this study, T_c was identified based on the onset of the diamagnetic transition in the real part of the AC susceptibility (χ'). Other techniques, such as resistivity measurements or alternative criteria applied to susceptibility data, might yield slightly different T_c values. While the obtained T_c is slightly lower than expected, it still falls within a reasonable range for Tl-2234-based materials.

3.2 Critical Current Density

The imaginary component of AC magnetic susceptibility (χ'') provides valuable information about energy dissipation mechanisms in materials, including eddy current losses, magnetic hysteresis, and magnetic flux dynamics under alternating fields [17]. Quantitative analysis of $\chi''(T)$ curves, particularly the position and field dependence of their maxima, enables determination of the critical current density (J_c) in superconducting materials. For measurements conducted at low frequencies, the temperature and field evolution of AC susceptibility is conventionally interpreted through critical-state models [18]. These theoretical frameworks describe the distribution of penetrated supercurrents, which flow at a density equivalent to the material's critical current density (J_c). A fundamental assumption in these models is that J_c depends solely on the local internal field (H_i) [11]. Bean's critical-state model, which simplifies the analysis by assuming J_c is H_i -independent, offers a direct methodology for extracting J_c values from



temperature-dependent χ'' measurements [19]. Within this framework, χ'' exhibits a maximum when the applied field achieves complete penetration of the superconducting volume, specifically at the point where shielding currents match the sample's maximum current-carrying capacity [20]. As illustrated in Figure 2, the temperature dependence of critical current density can be systematically calculated from these χ'' maxima. When an external magnetic field fully penetrates the entire volume of a superconductor, a condition is reached where the shielding currents become equivalent to the maximum carrier capacity (determined by hole concentration) or the bulk critical current density.

Figure 2. Temperature dependence of critical current density for the Tl-2234.

At the characteristic temperature T_p , corresponding to the maximum in the imaginary component of magnetic susceptibility (χ''), the penetration field H_p achieves complete sample penetration, reaching the center of the specimen. This penetration process can be quantitatively described using Bean's critical state model, which establishes a mathematical relationship between the critical current density J_c at the penetration temperature T_p and the penetration field H_p . This relationship has been well documented in previous studies [21-23], providing a fundamental framework for understanding the field penetration dynamics in superconducting materials.

$$J_c(T) = \frac{H_p}{R} \quad (2)$$

Equation (2) employs the parameter 'R', which is defined as the radius pertinent to the sample geometry. For cylindrical samples subjected to an axial magnetic field, 'R' directly corresponds to the cylinder radius, as detailed in reference [24]. However, for powder samples, 'R' necessitates interpretation as an effective average particle radius, as established in reference [25]. This distinction arises from the inherent morphological characteristics of powders, which are composed of non-spherical particles exhibiting a distribution of sizes and shapes. It is crucial to acknowledge that for powder samples, the application of equation (2) using an effective average particle radius introduces an approximation in the J_c calculation. A more precise determination of the average particle size would be advantageous for refining the accuracy of J_c calculations derived from equation (2). Such enhanced particle size characterization would enable a more faithful representation of the conductive pathways and superconducting volume fraction within the powder matrix. Subsequently, utilizing Equation (3), the critical current density was evaluated based on the peak position observed in the imaginary component (χ'') of the magnetic susceptibility. The critical current density J_c was calculated from the peak position of the imaginary part of AC magnetic

susceptibility χ'' (Eq. 1). The temperature dependence of critical current density for the studied sample demonstrates strong agreement with the scaling relation expressed in equation (3) [14]:

$$J_c(T) = J_c(0) \left[1 - \frac{T}{T_c}\right]^\alpha \quad (3)$$

Here, $J_c(0)$ represents the critical current density at absolute zero temperature (0 Kelvin) and α is the critical exponent. The critical current density value was obtained from the peak position. The solid line in Figure (3) shows the correlation between the experimental critical current density measurements as a function of temperature and equation (3) and the fitting parameters $J_c(0)$ and α were found to be $J_c(0) = 3.6 \times 10^5 \text{ A/cm}^2$ and $\alpha = 1.26 \pm 0.078$. The study findings align well with prior research on thallium-based superconductors,

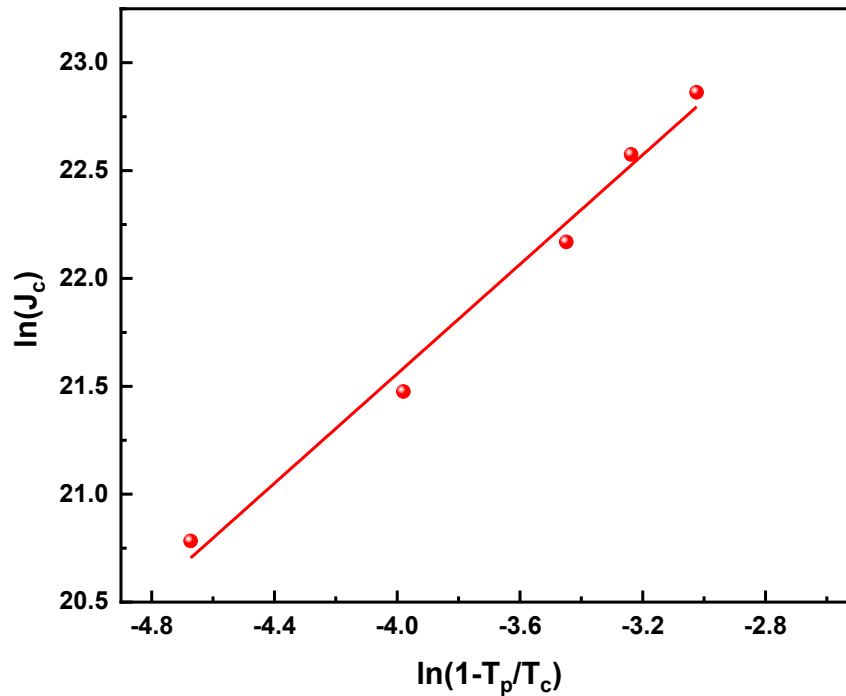


Figure 3. $\ln J_c(T)$ vs. $\ln(1-T/T_c)$ for the Tl-2234 sample. The slope of line determines the value of 'n' specific to sample.

highlighting the competitive superconducting characteristics of the Tl-2234 phase. Specifically, The observed critical current density $J_c(0) = 3.6 \times 10^5 \text{ A/cm}^2$ suggests the material is of good quality with strong pinning centers, which is typical for well-prepared thallium-based superconducting systems. The estimated critical current density at zero temperature, $J_c(0)$, for the Tl-2234 sample falls within the range of 10^5 to 10^6 A/cm^2 , consistent with the expected values for high-quality thallium-based superconductors. Reference [26] reports similar values for thallium cuprate superconductors, though measured at 77 K. In contrast, the $J_c(0)$ estimate in this study is extrapolated to 0 K, demonstrating that the obtained values align with the known high critical current properties of these materials, even at absolute zero. The measured $J_c(0) = 3.6 \times 10^5 \text{ A/cm}^2$ is consistent with other thallium cuprate systems, such as Tl-2223 with $J_c(0) = 3.0 \times 10^6 \text{ A/cm}^2$ [27] and Tl-1223 with $J_c(0) \approx 2.8 \times 10^5 \text{ A/cm}^2$. Additionally, The critical exponent $\alpha = 1.26 \pm 0.078$ further demonstrates consistency with established flux creep models for high-temperature superconductors, supporting both the Anderson-Kim flux creep model predictions and the expectations of collective creep theory (where the typical α range is 1.0 - 1.5) [28-31].

4. Conclusion

The AC susceptibility measurements revealed distinct behavior in both real (χ') and imaginary (χ'') components, demonstrating clear transitions between intragranular superconductivity and intergranular coupling in the Tl-2234 system. The sharp transition observed in the susceptibility curves, accompanied by minimal broadening in the transition region, indicates good sample quality and homogeneity. The systematic shift of χ'' peaks toward lower temperatures with increasing alternating magnetic field strength provides evidence for enhanced magnetic strength within the grains. This behavior is attributed to an increase in intra-grain pinning centers, resulting from a decrease in the superconducting volume fraction. Application of Bean's critical-state model to the AC susceptibility data enabled successful determination of the critical current density (J_c). The temperature dependence of J_c followed the empirical scaling relation

with remarkable precision, yielding a zero-temperature critical current density $J_c(0)$ of 3.6×10^5 A/cm² and a critical exponent of 1.26 ± 0.078 .

These findings contribute significantly to understanding the relationship between structural characteristics and magnetic properties in Tl-2234 superconductors. Future research directions could focus on optimizing synthesis conditions to further enhance the critical current density and investigating the effects of various dopants on the magnetic properties of this system.

References

- [1] M. J. Qin and S. X. Dou, Superconductors high T_c , in *Encyclopedia of Condensed Matter Physics*, vol. 2, 2024, pp. 565–579. <https://doi.org/10.1016/B978-0-323-90800-9.00254-7>
- [2] A. Molodyk and D. C. Larbalestier, The prospects of high-temperature superconductors, *Science*, vol. 380, no. 6651, pp. 1220–1222, 2023, doi: 10.1126/science.abq4137.
- [3] H. Wu, Recent development in high temperature superconductor: Principle, materials, and applications, *Applied and Computational Engineering*, vol. 63, pp. 153–171, 2024, <https://doi.org/10.54254/2755-2721/63/20241015>
- [4] R. Shipra, J. C. Idrobo, and A. S. Sefat, "Structural and superconducting features of Tl-1223 prepared at ambient pressure," *Supercond. Sci. Technol.*, vol. 28, no. 11, p. 115006, 2015, doi: 10.1088/0953-2048/28/11/115006
- [5] Effects of Tl content and magnetic field on phase formation of $Tl_mBa_2Ca_{n-1}Cu_nO_{2n+2+\delta}$ ($m=1$ and 2 , $n=4$) superconductors, *Physica C: Superconductivity and its Applications*. *Physica C: Superconductivity and its Applications*, vol. 586, p. 1353874, 2021, doi.org/10.1016/j.physc.2021.1353874.
- [6] B. Hassan, A. Alnakhilani, and M. Abdulhafiz, Investigating the effects of high magnetic fields on the phase stability of $Tl_2Ba_2Ca_2Cu_3O_{10-\delta}$ superconductor. *J. Phys. Sci.*, vol. 35, no. 2, pp. 33–45, 2024, doi: 10.21315/jps2024.35.2.3.
- [7] X. Chen and C. Gong, Dependence of the superconducting transition temperature on the type and number of CuO_2 layers in $Tl_2Ba_2Ca_{n-1}Cu_nO_{2n+4-\gamma}$.

Phys. Rev. B, vol. 59, no. 6, pp. 4513–4523, 1999, doi:
10.1103/PhysRevB.59.4513.

- [8] A. A. Khurram and N. A. Khan, A search for a low anisotropic superconductor, *J. Electromagnetic Analysis & Applications*, vol. 2, pp. 63–74, 2010, doi: 10.4236/jemaa.2010.22010.
- [9] K. Buchkov, A. Galluzzi, E. Nazarova, and M. Polichetti, Complex AC magnetic susceptibility as a tool for exploring nonlinear magnetic phenomena and pinning properties in superconductors, *Materials*, vol. 16, no. 14, p. 4896, 2023, doi: 10.3390/ma16144896.
- [10] G. Kovács, I. Kirschner, I. Halász, R. Laiho, T. Porjesz, K. Tompa, and G. Zsolt, Structure and superconductivity of variously prepared Tl-Ca-Ba-Cu-O compounds, *Journal of the Less Common Metals*, vol. 150, pp. 229–240, 1989, doi: 10.1016/0022-5088(89)90275-0.
- [11] K.-H. Müller, AC susceptibility of high temperature superconductors in a critical state model, *Physica C: Superconductivity*, vol. 159, no. 6, pp. 717–726, 1989, doi: 10.1016/0921-4534(89)90143-3.
- [12] L. E. Wenger, W. Win, C. J. McEwan, J. T. Chen, E. M. Logothetis, and R. E. Soltis, The complex AC susceptibility - critical current relationship in oxide superconductors, in *High- T_c Superconductors*, H. W. Weber, Ed. Boston, MA: Springer, 1988, ch. 40. doi: 10.1007/978-1-4899-0846-9_40.
- [13] A. V. Silhanek, S. Raedts, M. Lange, and V. V. Moshchalkov, AC-susceptibility of superconducting films with a periodic pinning array, *Physica C: Superconductivity*, vol. 408–410, pp. 516–517, 2004, doi: 10.1016/j.physc.2004.03.073.
- [14] E. Nazarova, A. Zaleski, and K. Buchkov, Doping dependence of irreversibility line in $Y_{1-x}Ca_xBa_2Cu_3O_{7-\delta}$. *Physica C: Superconductivity*, vol. 470, no. 9–10, pp. 421–427, 2010, doi: 10.1016/j.physc.2010.03.002.
- [15] M. R. Presland, J. L. Tallon, P. W. Gilberd, and R. S. Liu, "Bulk single-superconducting-phase thallium "2234" superconductor - $Tl_{2-x}Ba_2Ca_{3+x}Cu_4O_{12-\delta}$, *Physica C: Superconductivity*, vol. 191, no. 3–4, pp. 307–315, 1992, doi: 10.1016/0921-4534(92)90923-Z.

- [16] T. Kaneko, K. Hamada, S. Adachi, H. Yamauchi, and S. Tanaka, Synthesis of Tl-based “2234” superconductors, *J. Appl. Phys.*, vol. 71, no. 5, pp. 2347–2350, 1992, doi: 10.1063/1.351087.
- [17] R. B. Goldfarb, M. Lelental, and C. A. Thompson, "Alternating-Field Susceptometry and Magnetic Susceptibility of Superconductors, in *Magnetic Susceptibility of Superconductors and Other Spin Systems*, R. A. Hein, T. L. Francavilla, and D. H. Liebenberg, Eds. New York, NY: Plenum Press, 1991, pp. 49–80. doi: 10.1007/978-1-4899-2379-0_3.
- [18] C. P. Bean, "Magnetization of high-field superconductors, *Rev. Mod. Phys.*, vol. 36, no. 1, pp. 31–39, 1964, doi: 10.1103/RevModPhys.36.31.
- [19] F. Gömöry, Characterization of high-temperature superconductors by AC susceptibility measurements, *Supercond. Sci. Technol.*, vol. 10, no. 8, pp. 523–542, 1997, doi: 10.1088/0953-2048/10/8/001.
- [20] J. R. Clem, Granular and superconducting-glass properties of the high-temperature superconductors, *Physica C: Superconductivity*, vol. 153–155, pp. 50–55, 1988, doi: 10.1016/0921-4534(88)90491-1.
- [21] C. Lin, Bean's critical-state model as a consequence of the circuit model of non-linear resistance, *J. Appl. Phys.*, vol. 125, no. 3, p. 033901, 2019, doi: 10.1063/1.5084152.
- [22] C. Yang *et al.*, Improvement of critical current density J_c in powder-in-tube rapid heating, quenching and transformation Nb_3Al wires by doping with nano- SnO_2 , *Supercond. Sci. Technol.*, vol. 36, no. 6, p. 065001, 2023, doi: 10.1088/1361-6668/acc6f9.
- [23] J. Zhong, S. Zou, L. Lai, P. Chen, and S. Deng, Fast evaluation of the critical current of high-temperature superconducting coils based on the integral method, *J. Appl. Phys.*, vol. 132, no. 16, p. 163903, 2022, doi: 10.1063/5.0112003.
- [24] C. P. Bean, Magnetization of high-field superconductors, *Rev. Mod. Phys.*, vol. 36, no. 1, pp. 31–39, 1964, doi: 10.1103/RevModPhys.36.31.
- [25] M. W. Lee, M. F. Tai, S. C. Luo, and J. B. Shi, "Critical current densities in K_3C_{60}/Rb_3C_{60} powders determined from AC/DC susceptibility

- measurements, *Physica C: Superconductivity*, vol. 245, pp. 6–11, 1995, doi: 10.1016/0921-4534(95)00100-X.
- [26] M. Jergel, A. Conde Gallardo, C. Falcony Guajardo, and V. Strbik, Tl-based superconductors for high-current, high-field applications," *Supercond. Sci. Technol.*, vol. 9, no. 6, pp. 427–446, 1996, doi: 10.1088/0953-2048/9/6/001.
- [27] R. Awad, S. G. Elsharkawy, I. H. Ibrahim, and B. H. Chazbeck, Superconducting properties of (Tl_{1.6}Pb_{0.4})-2223 substituted by praseodymium, *Asian Journal of Applied Sciences*, vol. 2, pp. 63–73, 2009, doi: 10.3923/ajaps.2009.63.73.
- [28] A. N. Lykov, Magnetic flux creep in HTSC and Anderson-Kim theory, *Low Temp. Phys.*, vol. 40, no. 9, pp. 773–795, 2014, doi: 10.1063/1.4896968.
- [29] M. P. Maley, J. O. Willis, H. Lessure, and M. E. McHenry, Dependence of flux-creep activation energy upon current density in grain-aligned YBa₂Cu₃O_{7-x}, *Phys. Rev. B*, vol. 42, no. 4, pp. 2639–2642, 1990, doi: 10.1103/PhysRevB.42.2639.
- [30] J. R. Thompson *et al.*, Enhanced current density J_c and extended irreversibility in single-crystal Bi₂Sr₂Ca₁Cu₂O₈ linear defects from heavy ion irradiation, *Appl. Phys. Lett.*, vol. 60, no. 19, pp. 2306–2308, 1992, doi: 10.1063/1.107012.
- [31] S. S. P. Parkin *et al.*, Model family of high-temperature superconductors: Tl_mCa_{n-1}Ba₂Cu_nO_{2(n+1)+m} (m= 1, 2; n= 1, 2, 3). *Phys. Rev. B*, vol. 38, no. 10, pp. 6531–6535, 1988, doi: 10.1103/PhysRevB.38.6531.



Ab Initio Study of Structural, Thermal Stability and Electronic Properties of LiRuPO₄ Compound: A Storage Energy Application

Ahmed Memdouh Younsi¹, Mohamed Elbar², Saïd Khoudiri³

¹ University of Biskra, Laboratory of Physics of Photonics and Multifunctional Nanomaterials, BP 145, RP, 07000 Biskra, Algeria, Ahmed.younsi@univ-biskra.dz

² LAADI Laboratory, Faculty of Sciences and Technology, Ziane Achour University of Djelfa, P. O. B. 3117, Moudjbara Street, 17000 Djelfa, Algeria, m.elbar@univ-djelfa.dz

³ Electrical Engineering department, Faculty of Sciences and Technology, Ziane Achour University of Djelfa, P. O. B. 3117, Moudjbara Street, 17000 Djelfa, Algeria, s.khoudiri@univ-djelfa.dz

*Corresponding author: (A. M. Younsi), *Email Address:* Ahmed.younsi@univ-biskra.dz

Abstract

In this paper, we investigated the structural, electronic, and thermal stability of the LiRuPO₄ compound. We applied the ab-initio-density functional to conduct all our calculations. We used gradient generalized approximation with Hubbard correction implemented in the CASTEP (Cambridge Serial Total Energy Package) code. Results indicate that LRP crystallizes in the orthorhombic structure after phonons and thermal stability analysis. LRP is a semiconductor with an indirect gap after analysis of band structure curves within electronic properties and an energy gap of 2,18 eV. LiRuPO₄ will be an effective alternative to LiFePO₄ in storage energy applications such as electric batteries in vehicle fabrication technology.

Keywords: LiRuPO₄, density functional calculations, semiconductor, storage energy applications.

<https://doi.org/10.63070/jesc.2025.004>

Received 30 March 2025; Revised 29 April 2025; Accepted 15 May 2025.

Available online 22 May 2025.

Published by Islamic University of Madinah on behalf of *Islamic University Journal of Applied Sciences*. This is a free open access article.

1. Introduction

As the demand for electrical energy increases and the available sources are finite, efficient utilization of energy has become an important issue. In this regard, energy storage devices are required to ensure uninterrupted power supply and to regulate power generation. The lithium-ion battery is one of the smartest choices for energy storage devices due to its long charge/discharge cycling, low self-discharge, high energy density, and design flexibility. Improving the performance of lithium-ion batteries is a topic of interest, and numerous investigations have been performed to enhance the capacity and cycle stability of lithium-ion batteries. The cathodes of lithium-ion batteries are typically inorganic materials, and the most attractive cathode material is LiFePO_4 (LFP) due to its low cost and large operating voltage window. Although its operating voltage may be limited compared to NCM or LCO, these types of cathodes may fail explosively due to thermal runaway. LFP has better electronic conductivity than NCA and LCO. The poor electronic conductivity of pure LFP can be improved by cation and anion surface doping, and under optimum conditions, LFP shows about 10-11 orders of increased electronic conductivity. [1-3]

The driving force to study the LFP properties has been the significance of the ab-initio (DFT based) method available for studying the material properties down to the atomic scale level that links the material behavior at different length scales and the experimentation as well. Typically, available investigations were just based on experimental analysis. Various studies so far have been performed for LFP, like calculation of structural and electronic properties, effect of defects on the electrochemistry of LFP, lithium diffusion paths, electronic and ionic conductivities, etc.

In this work we studied a compound similar to LFP, which is LiRuPO_4 when we applied ab-initio study to calculation its structural, electronic and thermal stability properties of this compound. Lithium ruthenium phosphate, LiRuPO_4 , is a promising material for batteries in hybrid electric vehicles and for future nano-electronics, due to its stable ruthenium-redox potential and large lithium de-intercalation reaction occurring at a voltage around 3.5 V with respect to Li^+/Li . In an energy storage device, lithium is released (de-intercalated) from an electrode during the discharge process, where it reacts with an electrolyte phase and an electronic conductor to complete the intercalation reaction. [4, 5]

2. Computational Methods

The properties of LRP, including its structural, electronic, and thermal stability, were studied using ultra-soft pseudopotential plane waves in the CASTEP package [6]. The exchange-correlation potential was represented by the generalized gradient approximation of Perdew et al. with a Hubbard correction of 3 eV

(GGA-PBE+U) [7, 8]. The plane wave cut-off energy was set at 480 eV, and a $6 \times 6 \times 6$ special k-points mesh as per Monkhorst and Pack was used. Electrons and ions were relaxed when the variation of successive energies and forces exceeded 10^{-5} eV and 0.02 eV/Å, respectively. Energy convergence was considered achieved within an error of 10^{-5} .

3. Results And Discussion

3.1. Thermal Stability Properties

3.1.1. Phonons

Figure 1 shows stability thermal and energies are calculated as functions of the wave vector of phonons in the long-wavelength limit, and together these fold points become the complete phonon dispersion curves if extended over a whole reciprocal space of the appropriate size. In the frequency versus q-space plot (phonon curve), regions of linear dispersion correspond to frequencies of transverse phonons, while curvilinear dispersion corresponds to LA phonons. Branches with negative curvature also refer to (nonzero) low-frequency TA phonons. After the test of the stable crystal of LiRuPO₄, The positive range of the density phonon of states and phonon dispersion indicate that the orthorhombic structure in Pnma space group is the stable structure of LRP.

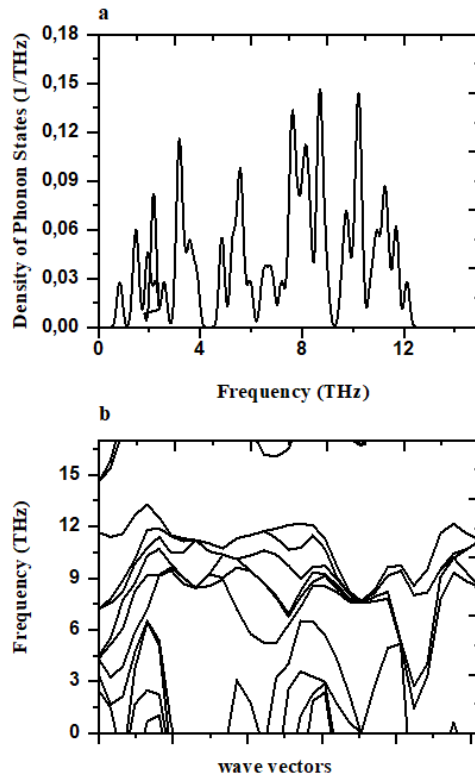


Figure 1. Phonons of LiRuPO₄ using GGA+U in Pnma orthorhombic structure.

3.1.2. Thermal Conductivity

In three-dimensional (3D) materials, the discussion of lattice thermal conductivity focuses on the transfer of phonon energy (see Figure 1). This energy transfer occurs through various mechanisms, including acoustic-optical interactions, regular and anharmonic processes, and Umklapp scattering, which are influenced by temperature and crystal structure. At low temperatures, research indicates that the thermal resistivity of these 3D crystals is proportional to the cube of the temperature, as explained by the Debye theory, which limits the density of states for phonons. Many studies prioritize thermal conductivity, a more practical parameter for applications that can be measured using experimental equipment. Generally, reducing thermal conductivity is essential for decreasing the thermal resistance of a given material. This

knowledge is often applied in technologies for electronic devices, among other uses. However, lithium-ion systems have more stringent requirements for these materials, particularly regarding the interaction between battery and thermal systems, due to the significant heat generated while cycling high-specific energy storage.

From the phonons curves, the thermal conductivity (κ_L) of LiRuPO_4 is typically compared with that of other conducting nitride-phosphates that have pyrophosphate-related structures. It is generally understood that in LiMPO_4 materials, the thermal conductivity decreases as the conductivity of heat or Li^+ carriers diminishes. At elevated temperatures, the κ_L of LiRuPO_4 is comparable to the values found in many mixed characteristic materials; however, it is lower than that of Li^+ -high-conducting sulfates and oxides. To date, the temperature dependence of the κ_L of LiRuPO_4 has not been investigated. Therefore, it is essential to extend the previously studied characteristics of κ_L in LiRuPO_4 to higher temperatures, considering both thermally and structurally related properties.

3.2. Structural properties

Lithium Ruthenium phosphate (LiFePO_4) was the first olivine type cathode material for rechargeable lithium batteries. However, this compound belongs to the Pnma orthorhombic space group, This structure (Figure2) consists of 6-coordinated PO_4 tetrahedra sharing corners with RuO_6 octahedra in edge-shared chains of corner linked LiO_6 octahedra that run along the a coordinate. The endo-octahedra of the Ru chains complete the orthorhombic coordination of the Li atoms. There is a direct correlation between the Li^+ diffusion and the low dimensional octahedral interstices present in the Pnma orthorhombic space group of the olivine structure. First-principles calculations converge to the orthorhombic cell parameters ; $a = 10.38 \text{ \AA}$, $b = 5.99 \text{ \AA}$, and $c = 4.78 \text{ \AA}$, see (table1) and to the mitigated atomic coordinates to the Pnma crystal structure, with Li1 atoms in (4f) positions $0,0,z$ with $z = 0.20$ and 0.327 , Ru (4c) in $0.555, 0.25, 0.247$, P in (4e) $0.918, 0.25, 0.728$, and O in (4d) at $0.276, 0.25, 0.255$ and $0.637, 0.25, 0.113$. Bond valence sum analysis of LiRuPO_4 , using 25 val, 1.04 vil, and 3.84 μB per Ruthenium ion, providing bond lengths between semiconductor and ligands between 2 and 3 Å .

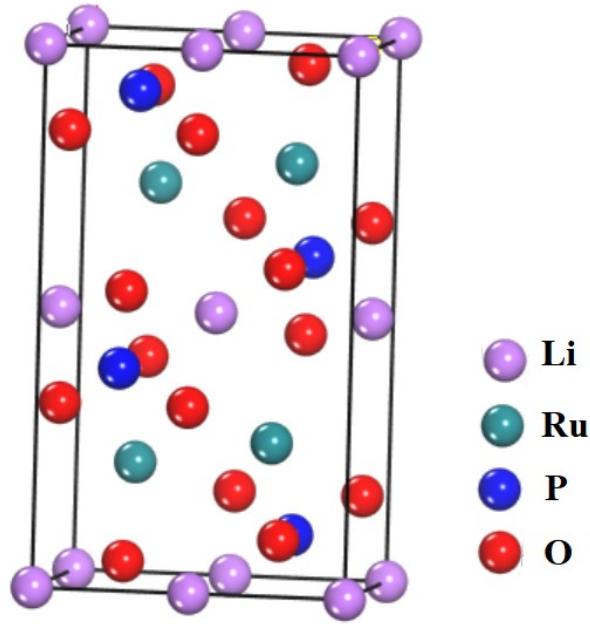


Figure 2. Primitive cell of LiRuPO₄ orthorhombic structure Pnma space group (No.62)

Table1. lattice parameter calculated of LiRuPO₄ in orthorhombic Pnma space group with using GGA+U (Hubbard correction U = 3.0 eV)

<i>Compound</i>	<i>Functional</i>	<i>Ground state energy (eV)</i>	<i>Lattice constants (Å)</i>	<i>Bulk modulus B₀(GPa)</i>
LiRuPO ₄	GGA +U	-18889,71	a=10,38 b=5,99 c=4,78 V=297,20A ^{o3}	236,62

3.3. Electronic properties

3.3.1 Band structures

The band structure of LiRuPO₄ has seen little theoretical focus, and that too via an effective one-electron single-electron-electron based theory. Here, using much more robust and rigorous computational quantum physics methods of GGA+U, we present in Figure3 the theoretical results of the band structure curves of

LiRuPO₄, The fermi level was fixed at 0 and we got indirect energy gap between two points in Brillouin zone, Z and X, the value of this gap is 2,18eV, so that LRP is semiconductor compound.

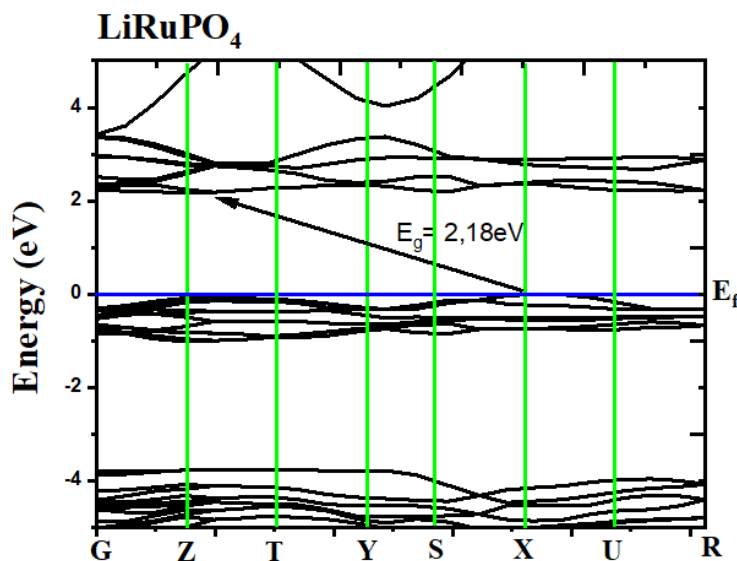


Figure 3. Band structure curve of LiRuPO₄ using GGA+U

4. Conclusion

In this study, ab initio calculations based on Density Functional Theory (DFT) were used to examine the thermal stability, structural, and electronic properties of LiRuPO₄. The study employed the pseudo-potential plane waves method, using a primitive cell instead of the standard approach. This method determined that the concentration window for the atomic distance of the orthorhombic phase olivine-LiRuPO₄ (LRP) was about 0.05–0.1 Å of Li atoms per unit cell of LRP, a finding that is higher than the reported insertion composition of Li for phase transformation of LRP, and has significant implications for the understanding of LRP's behavior. Additionally, the material LRP exhibited semiconductive behavior.

Our ongoing efforts to extend the duration of the two-stage reduction process are nearing completion. The charge-discharge kinetics, primarily influenced by the intercalation reaction of lithium, are a key focus. In future research, we are exploring atomistic modeling of high capacities in both the cathode olivine LiRuPO₄ and the anode ternary orthosilicate Li_{4-δ}Ru_{1-x}Ti_xPO₄. This development aims to achieve rapid charging by combining efficient 3D lithium migration with excellent electronic and ionic conductivities. We are also proposing an analytical method for developing high-capacity silicon-based anodes with significantly less experimental screening work. The key parameters relevant to the reversible capacitive

energy during the insertion process are under thorough study. After that, we have not forgotten the thermodynamics of the phosphate $\text{Li}_{4-\delta}\text{Ru}_{1-x}\text{Ti}_x\text{PO}_4$ olivine in comparison to lithium lithiated phosphate phases and oxide spinel, providing comprehensive insight into the chemical behavior of the metastable phase.

References

- [1] Al-Samet, M. A. M. M. & Burgaz, E., Improving the lithium-ion diffusion and electrical conductivity of LiFePO_4 cathode material by doping magnesium and multi-walled carbon nanotubes. *Journal of Alloys and Compounds*. 947 (2023) 169680.
- [2] Erabhoina, H. & Thelakkat, M. Tuning of composition and morphology of LiFePO_4 cathode for applications in all solid-state lithium metal batteries. *Scientific reports*. 12 (2022) 5454.
- [3] Suarso, E., Setyawan, F. A., Subhan, A., Ramli, M. M., Ismail, N. S., Zainuri, M., ... & Darminto. Enhancement of LiFePO_4 (LFP) electrochemical performance through the insertion of coconut shell-derived rGO-like carbon as cathode of Li-ion battery. *Journal of Materials Science: Materials in Electronics*, 32 (2021) 28297-28306.
- [4] Zhao, Q. F., Zhang, S. Q., Hu, M. Y., Wang, C., & Jiang, G. H. Recent advances in LiFePO_4 cathode materials for lithium-ion batteries. first-principles research. *International Journal of Electrochemical Science*, 16 (2021) 211226.
- [5] Zhang, B., He, Y., Gao, H., Wang, X., Liu, J., Xu, H., ... & He, X.. Unraveling the doping mechanisms in lithium iron phosphate. *Energy Materials*, 2(2022).
- [6] CLARK, S.J.; SEGALL, M.D.; PICKARD, C.J.; HASNIP, P.J.; PROBERT, M.J.; REFSON, M.I.J.; PAYNE, M.C. First principles methods using CASTEP. *Z. Krist.*,v. 220 (2005) 567.
- [7] PERDEW, J.P.; BURKE, K.; ERNZERHOF, M. Generalized Gradient Approximation Made Simple. *Phys. Rev. Lett.*,v. 77 (1996) 3865.
- [8] Shih, B.C., Yates, J.R. Gauge-including projector augmented-wave NMR chemical shift calculations with DFT+ U. *Phys. Rev. B*. 96 (2017) 1-10.

